



**HAL**  
open science

## International Benchmark on Numerical Simulations for 1D, Nonlinear Site Response (PRENOLIN): Verification Phase Based on Canonical Cases

Julie Regnier, Luis Fabian Bonilla, Pierre Yves Bard, Etienne Bertrand, F. Hollender, Hiroshi Kawase, Déborah Sicilia, Pedro Arduino, Angelo Amorosi, Domniki Asimaki, et al.

### ► To cite this version:

Julie Regnier, Luis Fabian Bonilla, Pierre Yves Bard, Etienne Bertrand, F. Hollender, et al.. International Benchmark on Numerical Simulations for 1D, Nonlinear Site Response (PRENOLIN): Verification Phase Based on Canonical Cases. Bulletin of the Seismological Society of America, 2016, 106 (5), pp.2112-2135. 10.1785/0120150284 . hal-01383223

**HAL Id: hal-01383223**

**<https://hal.science/hal-01383223v1>**

Submitted on 25 Mar 2024

**HAL** is a multi-disciplinary open access archive for the deposit and dissemination of scientific research documents, whether they are published or not. The documents may come from teaching and research institutions in France or abroad, or from public or private research centers.

L'archive ouverte pluridisciplinaire **HAL**, est destinée au dépôt et à la diffusion de documents scientifiques de niveau recherche, publiés ou non, émanant des établissements d'enseignement et de recherche français ou étrangers, des laboratoires publics ou privés.

1 International benchmark on numerical simulations for 1D,  
2 non-linear site response (PRENOLIN): verification phase  
3 based on canonical cases

4 Julie Régnier<sup>1</sup>

5 Luis-Fabian Bonilla, IFSTTAR, Paris, France

6 Pierre-Yves Bard, ISTERre, UGA,IFSTTAR, Paris-Grenoble, France

7 Etienne Bertrand, CEREMA, Nice, France

8 Fabrice Hollender, CEA, Cadarache, France

9 Hiroshi Kawase, DPRI, Kyoto University, Japan

10 Deborah Sicilia, EDF, Aix-en-Provence, France

11 Pedro Arduino, University of Washington, USA

12 Angelo Amorosi, Sapienza, University of Rome, Italy

13 Domniki Asimaki, Caltech, USA

14 Daniela Boldini, University of Bologna, Italy

15 Long Chen, University of Washington, USA

16 Anna Chiaradonna, University of Napoli, Italy

17 Florent DeMartin, BRGM, Orléans, France

---

<sup>1</sup> *Julie.regnier@cerema.fr, CEREMA, DTer Méditerranée, 56 Bd Stalingrad  
06300 Nice*

- 18 Marco Ebrille, Politecnico di Torino, Italy
- 19 Ahmed Elgamal, UCSD, San Diego, USA
- 20 Gaetano Falcone, Politecnico of Bari, Italy
- 21 Evelyne Foerster, CEA, Saclay, France
- 22 Sebastiano Foti, Politecnico di Torino, Italy
- 23 Evangelia Garini, NTUA, Athens, Greece
- 24 George Gazetas, NTUA, Athens, Greece
- 25 Céline Gélis, IRSN, Fontenay-aux-Roses, France
- 26 Alborz Ghofrani, University of Washington, USA
- 27 Amalia Giannakou, Fugro, Ankora, Turkey
- 28 James R. Gingery, UCSD, San Diego, USA
- 29 Nathalie Glinsky, CEREMA, Nice, France
- 30 Joseph Harmon, University of Illinois at Urbana-Champaign, USA
- 31 Youssef Hashash, University of Illinois at Urbana-Champaign, USA
- 32 Susumu Iai, DPRI, Kyoto University, Japan
- 33 Boris Jeremić, UCD, Davis, USA
- 34 Steve Kramer, University of Washington, USA
- 35 Stavroula Kontoe, Imperial College, London, England
- 36 Jozef Kristek, Comenius University of Bratislava, Slovakia
- 37 Giuseppe Lanzo, University of Rome, Italy

- 38 Annamaria di Lernia, Politecnico of Bari, Italy
- 39 Fernando Lopez-Caballero, Centrale Supélec Paris, France
- 40 Marianne Marot, CEREMA, Nice, France
- 41 Graeme McAllister, University of British Columbia, Canada
- 42 Diego Mercerat, CEREMA, Nice, France
- 43 Peter Moczo, Comenius University of Bratislava, Slovakia
- 44 Silvana Montoya-Noguera, Centrale Supélec, France
- 45 Michael Musgrove, University of Illinois at Urbana-Champaign, USA
- 46 Alex Nieto-Ferro, EDF, Clamart, France,
- 47 Alessandro Pagliaroli, CNR-IGAG, Rome, Italy
- 48 Federico Pisanò, Delft University of Technology, The Netherlands
- 49 Aneta Richterova, Comenius University of Bratislava, Slovakia
- 50 Suwal Sajana, University of Rome, Italy
- 51 Maria Paola Santisi d'Avila, UNS, Nice, France
- 52 Jian Shi, Caltech, USA
- 53 Francesco Silvestri, University of Napoli, Italy
- 54 Mahdi Taiebat, University of British Columbia, Canada
- 55 Giuseppe Tropeano, University of Cagliari, Italy.
- 56 Luca Verrucci, University of Rome, Italy

57 Kohei Watanabe, Shimizu Corporation, Tokyo, Japan.<sup>2</sup>

58

---

<sup>2</sup> The author's list involves first the seven organizers of the PRENOLIN project followed by the participants in alphabetic order.

## 59 **Abstract**

60 PRENOLIN is an international benchmark aiming to test multiple numerical simulation codes  
61 capable of predicting non-linear seismic site response with various constitutive models. One  
62 of the objectives of this project is the assessment of the uncertainties associated with non-  
63 linear simulation of one-dimensional (1D) site effects. A first verification phase (i.e.  
64 comparison between numerical codes on simple, idealistic cases) will be followed by a  
65 validation phase, comparing the predictions of such numerical estimations with actual strong  
66 motion recordings obtained at well-known sites. The benchmark presently involves 19 teams  
67 and 23 different computational codes.

68 We present here the main results of the verification phase dealing with simple cases. Three  
69 different idealized soil profiles were tested over a wide range of shear strains with different  
70 input motions and different boundary conditions at the sediment/bedrock interface. A first  
71 iteration focusing on the elastic and visco-elastic cases proved to be useful to ensure a  
72 common understanding and to identify numerical issues before pursuing the non-linear  
73 modeling. Besides minor mistakes in the implementation of input parameters and output  
74 units, the initial discrepancies between the numerical results can be attributed to (1) different  
75 understanding of the expression "input motion" in different communities, and (2) different  
76 implementations of material damping and possible numerical energy dissipation. The second  
77 round of computations thus allowed a convergence of all teams to the Haskell-Thomson  
78 analytical solution in elastic and visco-elastic cases. For non-linear computations we  
79 investigate the epistemic uncertainties related only to wave propagation modeling using  
80 different non-linear constitutive models. Such epistemic uncertainties are shown to increase  
81 with the strain level and to reach values around 0.2 (log10 scale) for a PGA of  $5\text{m/s}^2$  at the

82 base of the soil column, which may be reduced by almost 50% when the various constitutive  
83 models used the same shear strength and damping implementation.

84

## 85 **Introduction**

86 Including site effects in seismic hazard assessments requires the consideration, at some stage,  
87 of non-linear behavior of soils, which may greatly affect their dynamic response to strong  
88 motion and significantly modify their amplification behavior compared to weak motion  
89 (computed or measured). Even in areas of moderate seismicity, the hazard level at long to  
90 very long return periods (i.e., several thousands to tens of thousands years) may be large  
91 enough to generate significant strains in shallow, soft soil layers, which in turn leads to a  
92 degradation of their mechanical properties such as hysteretic behavior with reduction of shear  
93 stiffness/strength and increased energy dissipation (Bonilla et al., 2005; Iai et al., 1995;  
94 Ishibashi and Zhang, 1993; Seed, 1969; Vucetic and Dobry, 1991; Yu et al., 1993; Zeghal et  
95 al., 1995).

96 Such dependence of the dynamic soil response on the level of seismic loading, conventionally  
97 denoted as "non-linear effects" (Beresnev et al., 1995), involves rather complex mechanical  
98 processes, which may be grouped roughly in two main classes. The first is the degradation of  
99 the mechanical properties of the material, which is often characterized by a decrease in the  
100 shear stiffness and strength coupled with an increase in energy dissipation; while the second  
101 is related to pore pressure changes in water-saturated granular soils, linked with volumetric  
102 changes of the soil skeleton under shear stress, and may generate liquefaction in loose sandy  
103 soils. Our interest here focused on the first type of non-linearity, without any consideration of  
104 pore water pressure generation or liquefaction.

105 The first type of non-linear effect (i.e. without liquefaction) was identified by geotechnical  
106 earthquake engineering studies following the 1967 Caracas earthquake and further  
107 corroborated by observations after the 1989 Loma Prieta (Chin and Aki, 1991) and the 1994



108 Northridge (Field et al., 1998) earthquakes. Moreover, this was later confirmed both by  
109 laboratory tests and recordings obtained on "vertical arrays" with two or more accelerometers  
110 at different depths within the same borehole. For instance, a statistical analysis of the  
111 numerous recordings of the Japanese KiK-net network (Régner et al., 2013) concluded that,  
112 for Peak Ground Acceleration (PGA) levels exceeding  $0.75 \text{ m/s}^2$  (a rather moderate level) at  
113 an outcrop, there is a 40 % chance of observing a non-linear soil response, leading to  
114 significant modifications with respect to the linear, low-strain response. These changes  
115 generally imply a reduction of the response amplification of the signal's high-frequency  
116 content and often a slight-to-significant increase of its low frequency content. Therefore,  
117 linear soil response estimates cannot be considered as being systematically on the safe side,  
118 and on the other hand, the high frequency reductions may significantly contribute to the safety  
119 margins. As a consequence, the accuracy, robustness and reliability of non-linear site effects  
120 prediction directly impacts the estimation of seismic hazard and associated risks, especially at  
121 long return periods.

122 While a consensus has undoubtedly been reached on the existence of non-linear effects, their  
123 quantification and modeling remains a challenge. Indeed, numerous techniques have been  
124 proposed for the assessment of site effects in the linear domain using empirical and/or  
125 modeling approaches on a generic or site-specific basis. Conversely, empirical estimation of  
126 non-linear site effects is more limited, especially in moderate seismicity areas where the on-  
127 site instrumental approach can only be a long (to very long)-term investment. Aside from a  
128 generic approach based on existing recordings (Derras et al., 2012; Sandikkaya et al., 2013),  
129 the only presently possible way for site-specific estimates is thus numerical simulation.  
130 Obviously, such analysis must be preceded by a precise geotechnical and geophysical  
131 characterization of the underground structure, and the choice of a suitable non-linear  
132 constitutive model.

133 Given the complexity of non-linear behavior of soils, many constitutive models and codes  
134 have been developed for such simulations. When the deformation remains moderate (i.e.,  
135 smaller than about 0.1-0.3 %), the so-called "equivalent linear model", which is a linear  
136 approach with an iterative adjustment of visco-elastic properties (shear modulus and  
137 damping) to the local strain level, is often used and accepted in practice. However, when the  
138 strain level exceeds these values (i.e., above 0.2-0.5 %), which can occur in very soft soils  
139 and/or with very strong input motions, a complete non-linear modeling, with an appropriate  
140 constitutive law fed by the correct soil parameters is required. These models fall into two  
141 categories: relatively simple constitutive laws with few parameters, that cannot reproduce a  
142 wide range of loading/unloading paths; and more complex models with many parameters  
143 (sometimes exceeding 10), which can succeed in describing all possible behaviors, but with  
144 parameters that can be difficult to determine or calibrate.

145 The ability to accurately predict non-linear site responses has indeed already been the subject  
146 of two recent comparative tests. It was one of the targets of the pioneering blind tests initiated  
147 in the late 80's/early 90's, on 2 sites of Ashigara Valley (Japan) and Turkey Flat (California);  
148 however, those sites lacked strong motion records until the 2004 Parkfield earthquake during  
149 which the Turkey Flat site experienced a 0.3 g motion. Since the soils were fairly stiff, the  
150 nonlinearity was not very strong. A new benchmarking of 1D non-linear codes was thus  
151 carried out in the last decade, based on the Turkey Flat site and a few other sites with vertical  
152 array data (La Cienega, California; the KGWH02 KiK-net site in Japan, and Lotung in  
153 Taiwan). Its main findings, reported by Kwok et al. (2008) and in Stewart and Kwok (2009)  
154 emphasized the key importance of the way these codes are used and of the required in-situ  
155 measurements. Significant differences between records and predictions have been postulated  
156 as being due to an incorrect velocity profile (although it was derived from redundant borehole  
157 measurements), a non-1D soil geometry (non-horizontal layers), and imperfections /

158 deficiencies in the constitutive models, which were unable to represent the actual curves for  
159 stiffness reduction and damping increase. Another test was undertaken on the Euroseis  
160 European test site (Mygdonian graben near Thessaloniki, Greece) as part of the  
161 Cashima/E2VP project, which included two separate exercises on two-dimensional (2D) non-  
162 linear numerical simulation codes and three-dimensional (3D), linear simulation codes. The  
163 2D non-linear (NL) benchmark proved inconclusive, as major differences were found  
164 between the few considered codes, with multiple possible causes, i.e. 2D numerical scheme,  
165 damping implementation, and NL constitutive laws (see Foerster et al., 2015). Given the fact  
166 that the codes used for these tests are routinely used in engineering practice for predictions of  
167 non-linear site responses, especially for moderate seismicity countries lacking strong motion  
168 recordings, there is a clear need to conduct further tests in better controlled conditions, in  
169 particular with in situ and laboratory measurements for an optimal tuning of the non-linear  
170 parameters used in each code.

171 For this reason, the PRENOLIN project considers only 1D soil columns to test the non-linear  
172 codes in the simplest possible, though realistic, geometries. It is organized in two phases: (1)  
173 a verification phase aiming at a cross-code comparison on very simple (and "idealistic") 1D  
174 soil columns with prescribed linear and non-linear parameters; (2) a validation phase for  
175 comparison between numerical predictions and actual observations, for sites as close as  
176 possible to a 1D geometry (horizontal stratification), without liquefaction evidence and with  
177 already available sets of downhole and surface recordings for weak to very strong motions  
178 and later complemented by careful in-situ and laboratory measurements designed as close as  
179 possible to the participants requirements. The sites were selected within the Japanese KiK-net  
180 and PARI (Port and Airport Research Institute) accelerometric networks.

181 The purpose of this article is to present and discuss the results of the verification phase, with a  
182 special focus on the epistemic uncertainties associated with the constitutive laws and

183 numerical schemes of the simulation codes. The first section describes the 3 idealized soil  
184 columns and the requested computations, considering different boundary conditions (rigid /  
185 elastic base, associated respectively with within / outcropping reference motion). The next  
186 section lists the numerous teams that volunteered to participate in this exercise and the main  
187 characteristics of their codes. The simulation results are then presented and compared, first in  
188 the linear case (with and without attenuation), and then in the non-linear case for various input  
189 signals and levels, with a discussion in each case on the amount and origins of uncertainty.

## 190 **The canonical cases**

191 The verification phase of this project aims at establishing the similarity between the computed  
192 wave motions at the surface of a soil column affected by amplification using different  
193 numerical codes, quantifying the amount of code-to-code differences and, as much as  
194 possible, understanding them. The computed responses were compared with analytical  
195 solutions when available. Figure 1 summarizes the calculations performed during the  
196 verification phase, for the linear (elastic and visco-elastic), and non-linear cases. In the elastic  
197 and visco-elastic cases, for which analytical results are available and provided that all  
198 participants/users share a common understanding of the physical soil parameters to be used,  
199 no differences (or minor) in the results are expected. These first calculations are needed in  
200 order to ensure a proper predictability of the induced deformation (shear strain) for all soil  
201 and seismic wavefield properties. On the other hand, for non-linear cases, discrepancies  
202 between the different computations are expected: the goal is to identify their origins in  
203 relation to the constitutive models and/or the numerical schemes (or other possible issues), to  
204 quantify the associated epistemic uncertainty, and to reduce it to its minimum level as much  
205 as possible.

206 The experiment was designed around three 1D canonical cases, chosen to represent simple  
207 and idealistic soil conditions overlying stiff bedrock substrata:

208 1) Profile 1 (P1) is a shallow (20 m thick), homogeneous soil layer presenting a  
209 significant velocity impedance ratio at rock, with amplification in the intermediate  
210 frequency range [2-10 Hz].

211 2) Profile 2 (P2) is a thick (100 m) soil layer with S-wave velocity gradually increasing  
212 with depth, overlying a very stiff bedrock, with a low fundamental frequency (below 1  
213 Hz).

214 3) Profile 3 (P3) consists of two homogeneous layers with moderate velocity contrasts,  
215 overlying a very stiff bedrock, with expected amplification effects in the intermediate  
216 frequency range (2-10 Hz). The goal is to investigate non-linearity effects within both  
217 layers, since significant strains can develop at or near each interface.

218 Various reference motions are considered for each profile, from very simple signals intended  
219 to capture the basic physics of NL behavior (pulse like and cyclic, quasi-monochromatic  
220 signals with increasing amplitude), to realistic accelerograms. For the latter, two strong  
221 motions were selected with very different spectral content (high and low frequency contents),  
222 and scaled to three PGA levels, in order to generate a wide range of shear strain levels in the  
223 soil column.

224 These reference motions were applied at the bedrock level, with two boundary conditions  
225 representative of the actual case studies: in one case, the reference motion was considered to  
226 mimic the outcropping motion at the surface of the underlying bedrock ("elastic" condition),  
227 while in the other it was considered to mimic the "within" motion recorded by a virtual sensor  
228 at the sediment-bedrock interface ("rigid" condition).

229

## FIGURE 1

### 230 *Soil properties*

231 The properties describing the (1D) linear and non-linear soil behavior for each profile include  
232 elastic, visco-elastic and non-linear soil properties. They are displayed in Figure 1 and Figure  
233 2, and summarized in Table 1.

234 The basic characteristics of soil profiles (i.e., thickness, density and seismic waves velocities)  
235 were chosen in order to be representative of typical soil profiles. Values of P-wave velocity  
236 ( $V_P$ ) are derived from the profiles of S-wave velocity ( $V_S$ ) shown in Figure 2, using assumed  
237 values of Poisson ratio (0.4 for soil and 0.3 for bedrock). Profiles P1 and P3 exhibit constant  
238 seismic velocities in each layer, while P2 includes a velocity gradient with a regular increase  
239 from  $V_S = 150$  m/s at the surface to  $V_S = 500$  m/s at the soil-bedrock interface, according to  
240 the equation:

$$241 \quad V_S(z) = V_{S1} + (V_{S2} - V_{S1}) \left( \frac{z - Z_1}{Z_2 - Z_1} \right)^\alpha$$

242 *Eq 1*

243 where  $V_{S1} = 150$  m/s and  $V_{S2} = 500$  m/s are the shear-wave velocities at depths  $Z_1 = 0$  m and  
244  $Z_2 = 100$ m, respectively, and  $V_S(z)$  is the shear wave velocity at depth  $z$ ;  $\alpha$  is taken equal to  
245 0.25.

### 246 *Visco-elastic properties*

247 We only consider intrinsic material damping (Biot, 1956; Johnston et al., 1979; Leurser, 1997),  
248 without any additional component from scattering. Intrinsic attenuation can be quantified by  
249 the quality factor  $Q$  (more commonly used in seismology), or the damping ratio  $\xi$  (used in  
250 engineering seismology). Here  $Q$  and  $\xi$  are the quality factor and the damping ratio of the S-

251 waves. They are linked by the formula  $Q = 1/(2\xi)$ , and can be determined by the loss of  
252 energy over one wavelength. Pure elastic materials totally restore the seismic energy after  
253 deformation, and should therefore have infinite Q values; as the numerical codes used here  
254 require a finite value as input, the "elastic" case was computed with very high values of Q  
255 (very low  $\xi$ ) for both soil and bedrock ( $Q = 5000$ ). For visco-elastic and non-linear (soft)  
256 materials, the energy dissipation at low strain was constrained to vary according to  $V_s$ ,  
257 through the classical – never appropriately justified by measurements - relationship  $Q =$   
258  $V_s/10$ , or equivalently  $\xi = 5/V_s$  ( $V_s$  in m/s) (Olsen et al., 2003).

### 259 **Non-linear soil properties**

260 The non-linear properties of each layer were characterized using classical  $G/G_{\max}(\gamma)$  and  $\xi(\gamma)$   
261 curves, relating the decay of shear modulus ( $G$ ) normalized by the elastic shear modulus  
262 ( $G_{\max}$ ) and increase of damping  $\xi$  with the shear strain  $\gamma$ . Normally, we would expect to have  
263 available measurements from laboratory or field experiments to derive the necessary  
264 parameters for a given rheology model. However, in order to verify the ability of different  
265 models to take into account the same shear modulus reduction and damping ratio data and to  
266 simplify the canonical soil description, and also to start with an analysis of only the “code-to-  
267 code variability”,  $G/G_{\max}(\gamma)$  and  $\xi(\gamma)$  curves were constructed following a simple hyperbolic  
268 model based on the following equations:

$$269 \quad K_0 = (1 - \sin(\phi))OCR^{\sin(\phi)}$$

270 *Eq 2*

$$271 \quad \sigma'_m = \sigma'_v(1 + 2K_0)/3$$

272 *Eq 3*

273  $\tau_{\max} = \sigma'_m \sin(\phi)$

274 **Eq 4**

275  $\gamma_{ref} = \tau_{\max} / G_{\max}$

276 **Eq 5**

277  $G / G_{\max} = 1 / (1 + \gamma / \gamma_{ref})$

278 **Eq 6**

279  $\xi = \xi_{\min} + (\xi_{\max} - \xi_{\min})(\gamma / \gamma_{ref}) / (1 + \gamma / \gamma_{ref})$

280 **Eq 7**

281 where the control parameters are the friction angle  $\Phi = 30^\circ$ , the over-consolidation ratio  $OCR$   
 282  $= 1$  and the gravitational acceleration  $g = 9.81 \text{ m/s}^2$ . Only cohesionless material was  
 283 considered here, so that the shear strength  $\tau_{\max}$  is computed using the vertical stress and the  
 284 friction angle. Both,  $\sigma'_m$  and  $\sigma'_v$  are the effective mean and vertical stresses;  $\gamma$  is the shear  
 285 strain. The reference shear strain  $\gamma_{ref}$  corresponds to the strain for which  $G = 0.5G_{\max}$  (in the  
 286 hyperbolic model as describe above it is given by Eq 5),  $K_\theta$  is the coefficient of earth pressure  
 287 at rest, and  $\xi_{\min}$  and  $\xi_{\max}$  are the minimum damping values at very low strain (intrinsic material  
 288 damping considered above for the visco-elastic behavior), and the maximum at very high  
 289 strain, respectively.

290 Only one  $G/G_{\max}(\gamma)$  and  $\xi(\gamma)$  curves were provided for P1, five for P2 (increasing for each 20  
 291 m depth interval), and two for P3 (one for each homogeneous layer). We assume a constant  
 292 strength per soil layer for all soil models. They are illustrated in Figure 2. For P1 and P2, they  
 293 are fitting a hyperbolic curve defined by the low strain shear modulus  $G_{\max} = \rho V_s^2$  and the  
 294 shear strength  $\tau_{\max}$  at the center of each layer or sublayer. For P3 the  $G/G_{\max}(\gamma)$  and  $\xi(\gamma)$   
 295 chosen models were very similar to one another using the previous hyperbolic model. For P3,



296 the set of Darendeli models (Darendeli, 2001) was used and adjusted to a simple hyperbolic  
297 model as for P1 and P2; as Darendeli's models are defined only up to a maximum shear strain  
298 of 1 %, the P3 curves were defined by multiplying the shear strength  $\tau$  by factors 1.1 and 2 at  
299 depths of 10 m and 35 m, respectively, and the final curves were then computed based on the  
300 hyperbolic models associated to these values.

301 Some numerical codes include sophisticated constitutive models for NL soil behavior, which  
302 require very specific additional parameters, which should be consistent with the  $G/G_{max}(\gamma)$  and  
303  $\xi(\gamma)$  curves supplied for the other codes. The definition of these additional parameters was  
304 done individually by each team, with the following simple assumptions: the soil is  
305 cohesionless (i.e.  $c' = 0$  and Plasticity Index  $PI = 0$ ), the soil particle size distribution is  
306 defined with  $D_{10} = 0.2$  mm and  $D_{50} = 0.35$  mm, and a uniformity coefficient  $D_{60}/D_{10} = 1.8$ .

### 307 **TABLE 1**

### 308 **FIGURE 2**

## 309 ***Reference rock motion***

310 In the first phase of the project, each participant was provided (i) a simple Ricker pulse input  
311 motion derived analytically, and (ii) two real acceleration time histories scaled to three  
312 different PGA levels (0.5, 1 and 5 m/s<sup>2</sup>) to observe the evolution from linear to non-linear soil  
313 behavior. The two accelerograms were selected to be representative of very different  
314 frequency contents, in order to analyze its influence in the non-linear computations. Each  
315 accelerogram was pre-processed in the same way as explained further below. The Fourier  
316 transforms of the three normalized input motions are illustrated in Figure 3.

### 317 **The pulse-like input motion**

318 The Ricker pulse input motion corresponds to acceleration, velocity and displacement time-  
319 histories defined by equations (8) to (10). A central frequency of 4 Hz was chosen to produce

320 sufficient energy at the fundamental frequency of each of the three profiles, while having a  
321 broad band energy in the main bandwidth of earthquake geotechnical engineering, i.e. 1-10  
322 Hz.

$$323 \quad a(t) = [1 - 2(\pi t f_c)^2] \exp(-(\pi t f_c)^2)$$

324 *Eq 8*

$$325 \quad v(t) = t \exp(-(\pi t f_c)^2)$$

326 *Eq 9*

$$327 \quad d(t) = \frac{1}{-2(\pi f_c)^2} \exp(-(\pi t f_c)^2)$$

328 *Eq 10*

329 where  $f_c$  is the central frequency and  $a(t)$ ,  $v(t)$  and  $d(t)$  are the acceleration, velocity and  
330 displacement time histories, respectively. The acceleration time histories and the normalized  
331 Fourier Transform spectra for the three input motions are illustrated in Figure 3.

### 332 **Real reference input motions**

333 To investigate the effect of frequency content on the computation of non-linear soil behavior,  
334 we used two real input motions with different frequency contents recorded at rock outcrop  
335 sites. One has a predominant frequency of 11.4 Hz, and the other of 4.8 Hz: they are labeled  
336 hereafter HF and LF, respectively. The metadata of these two recordings are described in  
337 Table 2 and their acceleration, velocity and displacement time histories are illustrated in  
338 Figure 3. We can observe that the spectral shapes are quite different, the main energy of the  
339 signal for the LF motion lies between 0.5 to 10 Hz and for the HF motion between 5 to 20 Hz.  
340 The duration of the HF event is about 80 s while it is shorter for the LF motion around 15 s.  
341 In this work, we considered only the horizontal EW component of each recording.

342

**TABLE 2**

343 The velocity and displacement time histories of these two recordings were calculated from the  
344 original raw acceleration data, following this procedure: (1) removal of the mean, (2) zero  
345 padding of the signal by applying Boore's approach (Boore and Bommer, 2005) over a  
346 specific time duration corresponding to 20 s before the first, and after the last, zero-crossing  
347 of the original acceleration time series, (3) high-pass filtering of the signal, and (4) integrating  
348 twice to obtain consistent velocity and displacement time histories.

349

**FIGURE 3**

350

## 351 **Participants and tested numerical codes**

352 We compared 23 different numerical codes used by 21 participating teams, as listed in Table  
353 3. As some teams use several codes, each computational case/team is annotated by a letter and  
354 a number. Two or more teams used the same code, including Deepsoil (4 teams for the  
355 verification and 5 for the validation), FLAC (2 teams) and OpenSees (3 teams). Others used  
356 the same constitutive model, notably Iai's (1990) model (2 teams), Iwan's model (Ishihara,  
357 1996; Iwan, 1967) (4 teams) and the Hujoux model (Aubry et al., 1982) (2 teams). The  
358 participant teams were composed of people having different background and expertise, which  
359 can be relevant for analyzing the site response variability. Firstly, two disciplines are  
360 represented in this benchmark, seismology and geotechnical earthquake engineering and  
361 secondly, the participants are either developers or users.

362 We identified three different, non-exclusive code groups, according to three main  
363 characteristics: (1) the type of numerical scheme, (2) the way to implement the attenuation,  
364 either in the low strain range or in the large strain range, and (3) the type of non-linear  
365 constitutive models. Each of these three groups is detailed in the next sections.

366  
367  
368

### **TABLE 3**

#### 369 ***The numerical scheme***

370 The 20 codes that solve the problem in time domain are split in two main categories: two  
371 types of spatial approximations are considered:

372 (a) The Finite Element Method (FEM) is by far the most common, used by 18 teams and  
373 implemented in three different ways:

- 374 i) Standard method (ST.FEM), used by 12 teams: B-0, D-0, H-0, L-1, M-1, N-0, R-  
375 0, S-0, T-0, U-0, W-0 and Z-1.
- 376 ii) Spectral method (SP.FEM), used by 1 team: Q-0
- 377 iii) Discontinuous Galerkin method (DG.FEM), used by 1 team: Y-0.
- 378 (b) The Finite Difference Method (FDM) is used by 10 teams: A-0, C-0, E-0, F-0, G-0, J-  
379 0, K-0, L-2, M-0 and M-2;

380 The last remaining teams (J-1, T-1 and Z-0) consider the problem in the frequency domain  
381 and use a equivalent linear method involving linear, visco-elastic material with several  
382 iterations to tune the visco-elastic properties in each layer to the shear strain and modulus  
383 reduction and damping curves (Schnabel et al., 1972).

#### 384 ***Implementation of attenuation***

385 **Low strain attenuation:** At low strain levels (less than  $10^{-4}$ - $10^{-2}$  %), elasto-plastic  
386 constitutive models and most of the non-linear models have damping values close to zero,  
387 which is physically unrealistic, since all soil strata exhibit damping in the stress-strain plane  
388 even for weak deformations, indicating dissipation of energy.

389 In the frequency domain, implementation of a prescribed attenuation factor is relatively  
390 straightforward. In theory, fulfillment of the causality principle leads to a (slight) frequency  
391 dependence of the shear wave velocity, which should be specified (together with the damping  
392 value) at a specific frequency  $f_0$  (Aki and Richards, 2002) . However, this is not implemented  
393 in all codes: some consider a truly frequency-independent attenuation with a defined reference  
394 frequency for the velocity, while others dropped the causality principle and have frequency  
395 independent velocities.

396 In the time domain, attenuation can be approximated by implementation of a set of relaxation  
397 functions using rheological models such as the generalized Maxwell model (Blanch et al.,

398 1995; Day and Bradley, 2001; Day and Minster, 1984, 1984; Graves and Day, 2003) or  
399 modeled by a Rayleigh damping formulation. Both methods present pros and cons. The usage  
400 of rheological models to approximate attenuation is physical; however, it adds memory  
401 constraints to the computations. The greater the number of relaxation functions used, the  
402 better the attenuation factor will be approximated, although one should not use too many (see  
403 for example Peyrusse et al., 2014). On the contrary, the Rayleigh damping method is much  
404 easier to be implemented numerically; nevertheless, the parameters are not easily determined,  
405 and automatically involve a significant frequency dependence of  $Q$ . For low attenuation  
406 (below a damping ratio of 20%) it has been shown that Rayleigh damping and the generalized  
407 Maxwell model become equivalent (Semblat, 1997).

408 For the entire set of codes tested here, four kinds of attenuation implementations were used:

409 (1) Frequency-independent attenuation (frIA): Some model considered frequency  
410 independent attenuation instead of the use of the frequency dependent Rayleigh  
411 Damping/attenuation in the time domain analysis. Models A-0, E-0, K-0, Q-0, T-1 and  
412 Z-0 use series of Maxwell/Zener elements (Blanch et al., 1995; Day and Bradley,  
413 2001; Day and Minster, 1984, 1984; Graves and Day, 2003), which imply an almost  
414 constant attenuation over a specific, broad enough frequency range. Models F-0, J-0  
415 and M-2 used the frequency independent attenuation as proposed in (Phillips and  
416 Hashash, 2009a).

417 (2) Frequency-dependent attenuation (frDA), such as the Rayleigh damping (simplified or  
418 full), was used by 10 teams: B-0, G-0, H-0, L-1, M-0, M-1, R-0, S-0, T-0, W-0, Y-0  
419 and Z-1.

420 (3) Low strain frequency independent hysteretic damping (LSHD), was used by 4 teams:  
421 C-0, N-0, D-0 and R-0.

422 (4) Numerical damping (ND). Three teams (U-0, N-0 and D-0) use a variant of the  
423 Newmark integration scheme to simulate attenuation effects with purely numerical  
424 damping tools, while another team (L-1) used it to filter out numerical noise (NDfilt).

425

426 **High strain attenuation:** High strain attenuation can be computed directly from the  
427 hysteretic behavior of the soil subjected to strong ground motion (loading / unloading cycles).  
428 However, it was demonstrated it is difficult to reproduce simultaneously the specified  
429 decrease of  $G/G_{max}$  with increasing shear strain, and the increasing of damping. For this  
430 reason, a few teams (A-0, B-0, E-0 and T-0) chose to use a “damping control” (which implies  
431 a modification of the “Masing rules”, and is thus labeled as “no-Masing rules”): it is based on  
432 a mapping that converts a hysteresis loop in such a way that it will satisfy the hysteretic  
433 damping at the current strain level (Iai et al., 1992). Other teams (J-0) used the method  
434 proposed in Phillips and Hashash (2009a), which modifies the unload and reload paths of the  
435 extended Masing rules.

#### 436 *Non-linear constitutive models*

437 In geotechnical earthquake engineering, non-linear soil behavior is a well-established concept.  
438 In laboratory experiments, such as cyclic tri-axial tests, the non-linear soil behavior is  
439 expressed by hysteresis loops in axial stress-strain plots, which can be linked to shear stress-  
440 strain plots. The soil response under cyclic loading (representing seismic loading) depends on  
441 the properties of the cyclic loading (e.g. time history, peak amplitude) and on the soil  
442 properties (e.g. strength, relative density).

443 In non-linear models, the true hysteresis soil behavior is simulated by the use of constitutive  
444 models which mimic the experimental hysteresis curves, or the shear modulus decay  
445 ( $G/G_{max}(\gamma)$ ) and attenuation ( $\xi(\gamma)$ ) curves.

446 According to information gathered from each participant, the codes tested here are  
447 implemented with various non-linear models, including:

448 ⇒ Iai's model (Iai et al., 2011; Iai and Ozutsumi, 2005): B-0, E-0,

449 ⇒ MKZ modified hyperbolic model (Matasovic and Vucetic, 1993): A-0

450 ⇒ Cundall's model (Cundall, 2006): M-0

451 ⇒ Iwan's model (Ishihara, 1996; Iwan, 1967): K-0, Q-0, U-0, Y-0

452 ⇒ Logarithmic function model (Puzrin and Shiran, 2000) : L-1

453 ⇒ Modified Hujieux model (Aubry et al., 1982): D-0, N-0, S-0

454 ⇒ Multiyield model (Elgamal et al., 2003; Yang et al., 2003): H-0

455 ⇒ Extended Hyperbolic model (Phillips and Hashash, 2009) : F-0, H-0, J-0, M-2, T-0

456 ⇒ HSsmall (Isotropic hardening elasto-plastic soil model) (Schanz et al., 1999): Z-1

457 ⇒ Pisanò 3D Elastic-plastic model (Pisanò and Jeremić, 2014): R-0;

458 ⇒ BWGG: Extended Bouc Wen model (Gerolymos and Gazetas, 2005): G-0

459 ⇒ Modified extended hyperbolic model: C-0

460 ⇒ Manzari-Dafalias model: W-0 (Dafalias and Manzari, 2004)

461 In order to compare the different constitutive models, stress/strain controlled tests could have  
462 been conducted. However, some of the teams were not able to perform it. To overcome this  
463 difficulty, we asked the teams to compute nonlinear simulations with their codes on one of the  
464 idealized soil profiles (P1) with a sinusoidal input motion of increasing amplitude and with a  
465 rigid substratum base (Figure 4). The frequency of the input motion was low enough to avoid



466 any issues with wave propagation. Moreover, the result of this simulation was recorded at the  
467 node above the soil/bedrock interface, having a strength of 65 KPa.

468 The resulting plots are illustrated in Figure 5 for the total length of motion and in Figure 6 for  
469 a specific zoom on the first two cycles (blue for the first and red for the second).

470 The full duration of motion leads to very high strain levels (5%), and the stress-strain curves  
471 are highly variable from one computation to another. Even for a similar constitutive model,  
472 the curves can differ. For Iwan's model U-0 and Y-0 results are close to one another while  
473 different from K-0 and Q-0. The shape of the curves depends also on the use or not of  
474 damping control. For instance, teams A-0, B-0, D-0, E-0, J-0, T-0 and F-0 used damping  
475 control and all exhibit stress-strain curves with secant modulus degrading with strain.

476 Some teams could not follow the prescribed shear strength values (M-0, M-1, M-2, R-0, S-0,  
477 W-0) mainly because of depth dependency of the shear strength implemented in the code.  
478 They used very different values; the comparison of the corresponding stress-strain curve is  
479 thus irrelevant. Therefore, we looked at the first two cycles of motion that involve much  
480 lower strain (not exceeding 0.5%): the stress-strain curves are closer to each other, although  
481 some indicate larger hysteresis loop (B-0) or lower maximal shear strain (Z-1). This  
482 comparison helped to emphasize that hardwired built-in features on some NL codes, based on  
483 empirical correlations or geotechnical relations (between the shear strength and the confining  
484 pressure, for instance) prevent consideration of fully arbitrary sets of NL parameters.

485 **FIGURE 4**

486 **FIGURE 5**

487 **FIGURE 6**

## 488 ***Code usage protocols***

### 489 **Reference frequency for visco-elastic damping (Maxwell/Zener Model)**

490 Relatively little is known about low-strain, intrinsic attenuation in real soils. Its traditional  
491 implementation supposes frequency independent damping values. This is readily achieved  
492 using the Kelvin-Voigt model when solving the wave propagation in the frequency domain  
493 (Ishihara, 1996). Conversely, the Maxwell/Zener generalized body better describes anelastic  
494 material properties in both the time and frequency domain solution of wave propagation  
495 (Moczo et al., 2004). However, the use of this rheology implies a slight velocity dispersion to  
496 fulfill the causality principle. It is therefore necessary to carefully define a reference  
497 frequency for the reference velocity value, especially when different numerical methods are  
498 compared with one another (Peyrusse et al., 2014). *[This reference frequency must not be*  
499 *confused with the frequency bandwidth definition of the quasi-constant  $Q$  value used in the*  
500 *frequency independent attenuation method aforementioned, it should simply be within this*  
501 *frequency bandwidth.]*

502 A reference frequency was thus defined for each profile, at which common velocity and  
503 attenuation values were fixed. As indicated by some authors (Liu and Archuleta, 2006; Moczo  
504 et al., 2004) the values of reference frequency used in most cases is close to 1 Hz (as many  
505 3D computations including shallow, soft material, have rather low upper bound maximum  
506 frequencies). On the other hand, it is often suggested to select a frequency close to the  
507 frequency of interest. In our case, given the definition of the pulse-like motion, we chose a  
508 reference frequency of 4 Hz, i.e. the central value of the input wavelet.

### 509 **Definition and implementation of the reference motion**

510 We tested two base conditions at the sediment-substratum interface: (i) an elastic base, and  
511 (ii) a rigid base. The first condition corresponds to the usual hazard assessment studies, where

512 the rock ground motion is derived from deterministic or probabilistic analysis, and  
513 corresponds to the design motion at the surface of an outcropping rock. The second one  
514 corresponds to the case where a recording is obtained at depth within a down-hole array, and  
515 is used to derive the motion at surface or shallower depths. Depending on the communities or  
516 points of view, the implementation of input (or reference) motions into algorithms can be  
517 quite different, indicating that the terms "input motion" or "reference motion" are not  
518 understood in the same way by all the participants. For the seismological community, the  
519 input motion is often seen as the seismic signal carried by the up-going incident wave, while  
520 for the geotechnical community, it is often understood as the motion at a given reference rock  
521 site, resulting from the total-wavefield (up-going and down-going waves). This reference site  
522 may be either at the rock surface (it then includes the free-surface effect), or at depth (for  
523 instance the downhole sensor of a vertical array, which includes the interferences between the  
524 up-going and down-going waves) (Bonilla et al., 2002).

525 For the case of a perfectly rigid substratum, the reference input motion is the signal imposed  
526 at the soil-bedrock interface. This definition was clear among all teams. It was not so clear for  
527 the elastic substratum condition, whereby a more precise definition was required, since the  
528 greatest differences in the first round results came from different understandings of the term  
529 "input motion" by the various teams. The terminology must therefore be clearly stated:

530 - Outcrop motion: Seismic motion recorded at the surface and corresponding to free surface  
531 conditions in the outcropping rock. For 1-D cases, with vertically propagating plane seismic  
532 waves and homogeneous rock, this free-surface effect is simply a frequency-independent  
533 factor of 2, with respect to the up-going wave signal.

534 - Surface motion: Seismic motion recorded at the free surface of a sedimentary site and  
535 subjected to amplification effects.

536 - Within motion: Seismic motion recorded at depth, usually at a downhole site: in our case,  
537 this location corresponds to the interface between sediment and rock substratum (i.e.,  $z = 20$ ,  
538 100 and 50 m, for profiles P1, P2 and P3, respectively). This motion contains the total wave-  
539 field composed of the incident up-going and reflected down-going waves.

540 - Incident motion: Seismic motion that is carried by the incoming waves before they enter the  
541 sedimentary cover. In our case, it is the seismic motion carried by the vertically incident plane  
542 wave, and it cannot be directly measured.

543 Considering the confusion among the participants linked with different working traditions in  
544 different communities, we decided to use the concepts of “outcrop” and “within” input  
545 motions to define the "reference motion" at the downhole sensor, as recommended by Kwok  
546 et al. (2008) and Stewart and Kwok (2009). In linear/equivalent linear/non-linear site response  
547 analyses, two cases can be distinguished:

548 (1) if the reference motion is an outcrop recording, then one should use an elastic base  
549 condition with an up-going wave carrying a signal equal to exactly half the outcropping  
550 motion;

551 (2) if the reference motion is a within motion recorded by a downhole sensor, then one  
552 should use a rigid base condition without modifying the input motion.

553 In order to avoid any ambiguity, we will systematically use the expression "reference  
554 motion", which should be understood as detailed above for the elastic and rigid base  
555 conditions. Furthermore, this reference motion implicitly considers vertically incident plane S  
556 waves only. Finally, each team was free to choose the time step needed to fulfill the stability  
557 conditions of the used numerical scheme.

## 558 **Comparison of predictions**

### 559 *Methodology of comparison*

560 The participants were asked to compute the acceleration and stress-strain time histories at  
561 virtual sensors located at different depths within the soil profile. A total of ten virtual sensors  
562 were selected for each profile, with a depth interval equal to 1/10th of the total soil thickness:  
563 every 2 m for P1, every 10 m for P2 and every 5 m for P3. Acceleration and stress-strain  
564 values should be computed at staggered points: from the very surface for acceleration, and  
565 from half the depth interval for stress-strain values.

566 From the "raw" results provided by each participant, a comparative analysis was performed  
567 on the computed acceleration time histories, transfer function, 5% pseudo-response spectra,  
568 the depth distribution of peak shear strain and PGA, and the stress-strain plots at different  
569 depths. Such comparisons were done for each profile, for each computational case (linear vs.  
570 non-linear, elastic vs. visco-elastic soil behavior, and rigid vs. elastic substratum conditions)  
571 and for the different input motions.

572 For the sake of simplicity and conciseness, the main section of the present article presents  
573 results for only the P1 case. The P2 and P3 profiles are compared to P1 results in terms of  
574 variability of the surface motion only, but the conclusions are based on the results from all  
575 three profiles.

### 576 *Visco-elastic computations*

577 Figure 7 displays the comparison for the P1 profile of the surface acceleration for the pulse-  
578 like motion under an elastic substratum condition, for the linear elastic computation for a  
579 short window (3 s) of signal. All results converged towards the analytical solution calculated  
580 with the Haskell-Thomson method (Haskell, 1953; Thomson, 1950), but this was achieved

581 only after the second iteration. There were indeed unexpected and significant discrepancies in  
582 amplitude at the end of the first iteration, caused by: (1) inconsistent implementation and  
583 understanding of the term "input motion" (clarified as mentioned in the code usage protocols),  
584 (2) problems with units, or (3) representations of soil properties. During the first iteration,  
585 some phase discrepancies could be also identified, associated either to the assignment of the  
586 "input motion" at different depths some distance below the sediment/rock interface (which  
587 caused a constant time delay), or to increasing time delays at the end of the computed cycles,  
588 that were associated to numerical dispersion.

### 589 **FIGURE 7**

590 Figure 8 shows the results of visco-elastic computations of the acceleration at the surface of  
591 the pulse-like motion with a rigid substratum condition. The convergence was also obtained  
592 after the second iteration, with minor corrections (similar to the ones observed for the elastic  
593 case) and after having specified the reference frequency to be considered for the  
594 implementation of damping. We chose a reference frequency of 4 Hz, which is exactly the  
595 central frequency of the pulse-like motion (Figure 8)

### 596 **FIGURE 8**

597 These unexpected issues were corrected after the first iteration to ensure a satisfactory  
598 convergence. This should however raise our awareness on the possibility of such  
599 misunderstandings and resulting errors, when site response computations are asked without  
600 clear enough specifications about the definition of the reference motion.

### 601 ***Non-linear computations***

602 Once agreement between the model predictions was reached for simple, linear cases for which  
603 analytical solutions are available, the variability of the results of non-linear calculations can

604 be fully associated with differences in implementation of non-linear soil behavior. Each team  
605 chose its appropriate time step to fulfill the stability conditions of their numerical scheme. We  
606 acknowledge that this might be another cause for some discrepancies in the results, especially  
607 for strongly nonlinear cases, but such numerical issues are also one component of the code-to-  
608 code variability that is under investigation in this verification exercise.

609 Figure 9 compares the Fourier transfer functions (surface over reference bedrock motion) and  
610 Figure 10 compares pseudo-response spectra at the surface for the P1 profile, with a rigid  
611 substratum case. The subplots of these two figures illustrate the results for the high frequency  
612 (HF) waveform scaled to the lowest ( $0.5 \text{ m/s}^2$ ) and largest PGA ( $5 \text{ m/s}^2$ ) (a and c,  
613 respectively), and for the low frequency (LF) waveform scaled to the lowest and largest PGA  
614 ( $0.5 \text{ m/s}^2$  – b, and  $5 \text{ m/s}^2$ , d, respectively). The frequency content of the input motion and the  
615 scaling of the input motion prove to have a large influence on the non-linear soil behavior in  
616 the numerical simulations, and consequently on the variability of the results.

617 While the results from all teams exhibit a very satisfactory similarity (with larger differences  
618 than for the visco-elastic case) for the HF waveform scaled to the lowest PGA (a), differences  
619 between the model predictions are much greater for the highest PGA (c). This observation is  
620 more pronounced when looking at the LF input motion. Even for the lowest PGA (b), the  
621 variability increases significantly compared to the HF input motion, and it becomes very large  
622 for the large amplitude LF motion (scaled to  $5 \text{ m/s}^2$ , d).

623 The amount of variability between the results has been quantified through the calculation of  
624 the standard deviation (in  $\log_{10}$  units) for each frequency value and is illustrated in Figure 11.  
625 The variability is greater for the low frequency content input motion scaled to the highest  
626 PGA except close to the first frequency peak of the linear transfer function. As expected,  
627 strong non-linear soil behavior during this solicitation shifts the first frequency peak of the

628 transfer function to the low frequencies. The variability of the transfer function is similarly  
629 shifted.

630 Such variability is strongly linked to the peak shear strain reached in the soil column. For the  
631 LF input motion scaled to the highest PGA, the threshold shear strain above which the  
632 numerical simulations can no longer be considered as reliable (according to their authors),  
633 was reached by some codes. Indeed, some teams (L-1 and Z-0) consider a maximal reliable  
634 deformation between 1 to 2%; while others consider their code to work well over a wide  
635 range of deformation and are limited by the dynamic soil properties resolution only. For the  
636 computations using the HF and LF motions scaled to the highest PGA, we observe that the  
637 two equivalent linear methods (J-1 and Z-0) exhibit a very high de-amplification beyond 7  
638 Hz, compared to other simulations, which shows the classical over-damping limitation of that  
639 method. For the last two cases (HF and LF accelerograms scaled to 5 m/s<sup>2</sup>), the peak shear  
640 strain values are illustrated in Figure 12. It was calculated for each code/team couple, and for  
641 all the 10 sensor depths of the P1 profile. The largest peak strain values, largely exceeding  
642 1%, are reached at the deepest points for the LF input motion, while it remains about 10 times  
643 smaller (max 0.3%) for the HF motion, despite the identical PGA values on the input motion.  
644 Besides, given the shape of the  $G/G_{\max}$  and  $\xi(\gamma)$  curves, one may notice that the frequency-  
645 content of the input motion induced variability in the peak shear strain results which  
646 corresponds to an even larger variability in the  $G/G_{\max}$  and  $\xi(\gamma)$  values. For instance, at 7m  
647 depth, the peak shear strain for the LF motion is between 0.02 to 1% while it is between 0.03  
648 to 0.1% for the HF motion. This means the  $G/G_{\max}$  varies from 0.28 for the LF motion to 0.8  
649 for the HF motion. Thus, one may understand that the results will be very sensitive to the  
650 details of the constitutive model and the way that  $G/G_{\max}$  and  $\xi(\gamma)$  curves are approximated.

651 Incidentally, one may also notice that for P1, the peak shear strain occurs at the deepest point,  
652 close to the sediment/bedrock interface. Indeed, wave propagation in nonlinear media is the



653 cumulative effect of impedance contrast at the soil-bedrock interface, material strength, and  
654 intensity of the input motion. These combined effects make it difficult to analyze these results  
655 even when they are numerical and consider simple soil geometry.

656 **FIGURE 9**

657 **FIGURE 10**

658 **FIGURE 11**

659 **FIGURE 12**

## 660 **Epistemic uncertainty**

### 661 *Quantification of the variability of the results*

662 We quantified the variability between the simulations by the standard deviations (log10 units)  
663 of several ground motion intensity parameters, starting with PGA values [ $\sigma_{\text{PGA}}$ ], and then  
664 considering pseudo-response spectrum ordinates at different periods [ $\sigma_{\text{PSA}(T)}$ ], peak strains  
665 [ $\sigma_{\gamma_{\text{max}}}$ ], and a few energy related quantities.

666 The PGA values at the surface are first compared with the empirical variability (i.e. single  
667 station, within-event variability " $\Phi_{\text{SS}}$ "). Figure 13 illustrates the evolution of  $\sigma_{\text{PGA}}$  for the  
668 surface site of P1 for the 5 different computational cases and the different reference motion  
669 and boundary conditions. These are the linear-elastic, the linear-visco-elastic, and the non-  
670 linear computations with the input motions scaled to the lowest ( $0.5 \text{ m/s}^2$ ), intermediate ( $1$   
671  $\text{m/s}^2$ ) and highest ( $5 \text{ m/s}^2$ ) PGA. The  $\sigma_{\text{PGA}}$  is calculated for the pulse-like, the HF and the LF  
672 motions. The left subplot displays the results for the rigid substratum case (reference motion =  
673 within motion at sediment-basement interface), while the right subplot stands for the elastic

674 substratum case (reference motion = outcropping rock motion). The most striking features of  
675 these plots can be summarized as follows:

- 676 a) the (almost) systematic increase of  $\sigma_{\text{PGA}}$  with increasing PGA level, whatever the input  
677 signal and the type of boundary conditions
- 678 b) the (almost) systematically larger values of  $\sigma_{\text{PGA}}$  for the LF input motion compared to  
679 the HF input motion case (around twice as great for the three PGA values) : this  
680 corresponds to the higher strains generated by the LF motion. A similar plot as a  
681 function of peak strain instead of peak ground acceleration would exhibit a larger  
682 continuity between results of both input waveforms
- 683 c) the larger  $\sigma_{\text{PGA}}$  values for non-linear computations compared to the linear case (except  
684 for the very specific case of linear-elastic response with rigid boundary conditions,  
685 discussed later)
- 686 d) the maximum obtained  $\sigma_{\text{PGA}}$  value (0.15) remains below the specific single-station,  
687 within-event variability  $\Phi_{\text{SS,PGA}}$  value for a site with a  $V_{\text{S30}}$  equivalent to P1  
688 (Rodriguez-Marek et al., 2011), which is around 0.2. The uncertainties linked with the  
689 NL simulations remain below the “natural” single site response variability (at least for  
690 PGA values not exceeding  $5 \text{ m/s}^2$  and the very peculiar and simplified input wavefield  
691 considered here, consisting of pure vertically incident plane S waves. The latter one  
692 however includes the sensitivity to the characteristics of the incident wavefield, which  
693 is not accounted for here as only vertically incident plane waves are considered.  
694 Nonetheless, the use of PGA as a main metric is not enough. It is helpful to use  
695 spectral accelerations at other periods as well.

696 Our results indicate an exceptionally high  $\sigma_{\text{PGA}}$  value for one linear computation, the linear-  
697 elastic one with the HF reference motion and rigid boundary conditions. This computational  
698 case is the simplest but also the most demanding for a propagating seismic wave. Considering

699 that no seismic attenuation (damping) is considered for this specific computation (in the  
700 material or in the substratum), some codes usually use numerical attenuation to control real  
701 motion amplitudes. Thus, the high uncertainty observed here reflects variability in the  
702 implementation of the numerical damping for each code/team couple, together with the high  
703 sensitivity to the configuration, with a non-zero Fourier content of the reference motion at  
704 depth, at a frequency where destructive interferences between up-going and down-going  
705 waves should result in a null motion.

### 706 **FIGURE 13**

707 We then explored the variability of various seismic intensity measures: (i) the response  
708 spectra at the surface (SA) at three different periods (0.1, 1 and 3 s), (ii) the peak shear strain  
709 at the bottom of the sediment layer ( $\varepsilon$ ), (iii) the Cumulative Absolute Velocity (CAV), (iv) the  
710 Arias Intensity (IA), (v) the root mean square acceleration (Arms), and (vi) the 5%-95%  
711 Trifunac-Brady duration (DT). The tendencies are quite similar for the HF and LF motions,  
712 but are sensitive to the sediment/substratum limit condition (elastic vs. rigid). Considering  
713 that  $\sigma_{\text{PGA}}$  is greater for the LF motion, we choose that motion to illustrate the results in Figure  
714 14. For the rigid substratum case (left subplot), three groups of intensity parameters can be  
715 identified. The first group is composed of duration-dependent intensity parameters, i.e., CAV,  
716 IA and DT, which exhibit the largest  $\sigma$  values. The second group is composed of acceleration  
717 parameters (PGA, SA(T), Arms) and characterized by a lower  $\sigma$ , especially for long period  
718 [SA (T = 1 s)]. The third group consists only of the peak strain, with generally intermediate  $\sigma$   
719 values, which however exhibit the largest variability from one case to another. These three  
720 groups can also be distinguished in the elastic substratum case (right subplot), for which the  
721 largest case-to-case variability is also observed for the peak strain, exhibiting the highest  $\sigma$  for  
722 the highest PGA values. The duration-dependent parameters of the first group are less  
723 variable under elastic boundary conditions especially at low to intermediate PGA levels and

724 in the linear domain: rigid base conditions are very demanding for low damping materials,  
725 which maps much more on duration than on peak values.

726 **FIGURE 14**

727 The other profiles provided similar results as to the variability of predictions. As an example,  
728 Figure 15 compares the PGA variability, for the LF motion and a rigid substratum case, for  
729 the three profiles. The trends are similar for the three profiles: similar  $\sigma$  values, same  
730 tendency to increase with PGA. These results also stand for the elastic substratum case, as  
731 well as the fact that the variability  $\sigma$  is lower for the HF motion for the three profiles, by about  
732 a factor of two compared to the LF motion.

733 **FIGURE 15**

### 734 ***Origins of the variability: Can it be reduced?***

#### 735 **Definition of Groups and Sub-groups**

736 We considered four a priori ways to group the results according to some characteristics of the  
737 numerical codes: (G1) implemented attenuation method, (G2) numerical scheme, (G3)  
738 constitutive model, (G4) shape of the hysteretic curve according to (1) the ability to represent  
739 the actual shear strength value (here at the bottom of P1), and (2) the use or not of Masing  
740 rules for the loading/unloading path (damping control or not). Each group is further sorted  
741 into several sub-groups as follows.

742 Case G1 concerns the implementation of linear, intrinsic damping, as defined in the first part  
743 of this article. It is sub-divided into 3 sub-groups: (i) G1a: frequency-independent attenuation  
744 (A-0, E-0, F-0, J-0, J-1, K-0, M-0, Q-0 and Z-0), (ii) G1b: Rayleigh damping (B-0, G-0, H-0,  
745 L-1, M-1, R-0, S-0, T-0, W-0, Y-0 and Z-1), and (iii) G1c: low strain hysteretic damping (C-  
746 0, N-0, D-0 and R-0).

747 Case G2 is based on the numerical discretization scheme, which is sub-divided into 2  
748 subgroups: (i) G2a: finite-element (B-0, D-0, H-0, L-1, M-0, N-0, Q-0, R-0, S-0, T-0, U-0,  
749 W-0, Y-0 and Z-1), and (ii) G2b: finite-difference (A-0, C-0, E-0, F-0, G-0, J-0, K-0, L-2, M-  
750 2). A third sub-group could be considered G2c: consisting of equivalent linear codes working  
751 in the frequency domain (J-1 and Z-0).

752 Case G3 is based on the constitutive model. To ensure sufficient teams within each group, we  
753 split the code/team couple into 4 sub-groups according to the main constitutive model used:  
754 (i) G3a: Iai's model (B-0, E-0, Q-0), (ii) G3b: Iwan's model (K-0, L-1, U-0, Y-0), (iii) G3c:  
755 Philips and Hashash's model (F-0, J-0, L-2, M-2, T-0), and (iv) G3d: all other models.

756 Case G4 is based on the shape of the hysteresis loop according to (1) the shear strength used  
757 by each code/team couple and (2) the use of Masing rules or not for the loading/unloading  
758 path.

759 In the "canonical" models initially designed by the organizing team, the soil shear strength  
760 profile was assumed to be constant with depth in each soil layer, and had prescribed modulus  
761 reduction and damping curves. However, in most real situations, the shear strength should  
762 increase with depth. Even though these profiles were considered as "idealized" and simply  
763 intended to perform these verification tests, some teams felt very uncomfortable with this  
764 unrealistic assumption and decided to change the shear strength profile, by introducing a more  
765 realistic increase in shear strength with depth, having nevertheless, the imposed strength  
766 values at the center of each layer. Consequently, the actual non-linear soil parameters  
767 considered by each team were not identical, which is certainly responsible for part of the final  
768 variability observed, especially for large ground motions, for which the actual strain and  
769 damping are more sensitive to the shear strength than to the shear velocity, particularly at or  
770 close to major interfaces. For this reason, we further sorted each code/team couple into 2 sub-

771 groups, by analyzing the stress-strain plots for the LF motion and the highest PGA at the  
772 bottom of P1 (illustrated in Figure 16). We choose this computational case because it is the  
773 most challenging in terms of maximal shear strain reached in the soil column and therefore  
774 can highlight the differences between the computations. We found the following sub-groups:  
775 (i) shear strength is equal to 65kPa, as stated by the organizing team (A-0, B-0, C-0, E-0, F-0,  
776 G-0, H-0, K-0, Q-0, U-0, T-0, Y-0), and (ii) all others that exceeded this value (D-0, J-0, J-1,  
777 L-1, N-0, M-0, M-1, M-2, R-0, S-0, W-0, Z-0, Z-1).

778 In addition, we also consider the damping control implementation, (or in other words the use  
779 or not of the Masing loading/unloading rules). It has a major influence on the hysteresis  
780 curves and hence on the non-linear soil behavior, also illustrated in Figure 16. It is split into 2  
781 sub-groups: (i) damping control is used, i.e. the Masing rules are not applied (A-0, B-0, E-0,  
782 F-0, J-0, M-2), and (ii) no damping control used (all other teams).

783 Combining these two last parameters we end-up for G4 with three subgroups as follow: (i)  
784 G4-a: Specified shear strength and use of damping control (A-0, B-0, E-0, F-0, T-0), (ii) G4-  
785 b: Specified shear strength and no use of damping control and (C-0, G-0, H-0, K-0, Q-0, U-0,  
786 Y-0) (iii) G4-c: Different shear strength (D-0, J-0, J-1, L-1, N-0, M-0, M-1, M-2, R-0, S-0,  
787 W-0, Z-0, Z-1).

## 788 **FIGURE 16**

### 789 **Variability within the sub-groups**

790 Considering the level of code-to-code variability, and its increase with PGA or strain level, a  
791 major issue regarding non-linear computations is whether such variability, i.e. the uncertainty  
792 in the predicted motion, is intrinsic to these kinds of calculations, or can be reduced, and in  
793 the latter case, how? We thus looked at the variability within each subgroup of the four main  
794 groupings, in order to identify those which are associated to a significantly reduced scatter.

795 The standard deviations ( $\sigma_{log}$ , calculated in  $log_{10}$  units) of three parameters describing the  
796 computed surface accelerations and the strain levels at the bottom of P1, were used as metrics  
797 to validate the ability of a given grouping item to reduce the scatter of results. These  
798 parameters are the surface PGA and the acceleration response spectra (RS) at periods 0.3 s  
799 and 0.09 s (corresponding to P1's first and second resonance frequencies, respectively). For  
800 each, the variability was measured within each subgroup of the 4 groups. If the groupings are  
801 physically relevant, the within-subgroup variability should be significantly reduced.

802 Figure 17 shows the standard deviation values for each sub-group in each group (G1, G2, G3  
803 and G4) relative to the general standard deviation (all unsorted code/team couples) illustrated  
804 by the dotted gray line. The standard deviation of the PGA, response spectra at two periods  
805 and maximal deformation are calculated on the results for the profile P1, with the rigid  
806 substratum case and using the low frequency input motion scaled to the highest PGA (i.e. the  
807 motion that induces the strongest deformation in the soil column).

808 G1 and G2 (i.e. low strain attenuation and numerical scheme implementation, respectively) do  
809 not exhibit much lower  $\sigma_{log}$  values compared to the general  $\sigma_{log}$ , except for the lowest PGA  
810 input motion. Conversely, G3 to G4 (i.e. constitutive model, shear strength and damping  
811 control groups) do show reduced  $\sigma_{log}$  relative to the general  $\sigma_{log}$ , with G4 demonstrating the  
812 strongest reductions (by at least a factor of 2).

813 We can therefore conclude that (i) the shear strength is a key parameter for non-linear  
814 computations, and (ii) the constitutive model has a large influence; however (iii) the use (or  
815 not) of Masing rules appears to have an even greater influence for strong input motion.

816

### **FIGURE 17**

817 Figure 18 compares the pseudo-acceleration response spectra at the surface of the P1 profile  
818 with a rigid substratum condition subjected to LF and HF input motions scaled at the medium

819 (1m/s<sup>2</sup>) and highest (5 m/s<sup>2</sup>) PGA levels. The response spectra are sorted according to the G4  
820 sub-grouping, and the associated  $\sigma_{log}$  is represented by the thin lines on top of each subplot  
821 (the numbers on the right side indicate the number of code/team pairs in each sub-group). G4  
822 enables a clear distinction of the response spectra; particularly for the most demanding LF  
823 input motion. The  $\sigma_{log}$  values from the two sub-groups with identical  $\tau_{max}$  (G4a and G4b) are  
824 considerably reduced below 2 s, compared to the rest of the computations (G4c). This period  
825 bandwidth is relative to the PGA of this LF input motion. Similarly, for the HF input motion,  
826 the  $\sigma$  is reduced below 1 s.

827 Besides, the response spectra computed for the strongest input motions (HF and LF) at the  
828 surface of groups G4a and G4b are significantly different one to another which shows the  
829 large impact of using damping control or not. The response spectra computed with damping  
830 control are more damped at intermediate frequencies (period between [0.2 to 0.7] s and [0.2 to  
831 1] s for the HF and LF motion respectively) and less attenuated at low frequencies (periods  
832 greater than 0.7 and 1 s for the HF and LF motion respectively).

833 **FIGURE 18**

## 834 **Conclusions**

835 In the PRENOLIN's verification phase, the linear computation involving a simple pulse-like  
836 (Ricker) input motion proved to be very useful in understanding and eliminating some of the  
837 discrepancies between the different numerical codes that were compared. It was found that  
838 code-to-code differences can be attributed to three different sources: (1) minor mistakes in  
839 input parameter implementation or output units, (2) different understanding of the expression  
840 "input motion" within different communities, and (3) different intrinsic attenuation and  
841 numerical integration implementations. This benchmark showed that any nonlinear code



842 should be tested with simple linear cases before going into nonlinear computations to ensure  
843 the proper implementation of the elastic soil parameters.

844 Most of the codes tested in this verification benchmark were designed mainly for non-linear  
845 computations. Therefore, although the codes should well reproduce the soil behavior at low  
846 strains, their actual performance is mainly tested for their soil behavior predictions during  
847 strong shaking in real cases.

848 The results obtained so far indicate a code-to-code variability, which increases with the shear  
849 strain level (which in turn depends on both the PGA level, stiffness of the soil and the  
850 frequency content of the reference input motion). For example, for the low frequency input  
851 motion, at low PGA values ( $0.5 \text{ m/s}^2$ ) at the base of the soil column, the standard deviation is  
852 0.065 in logarithmic units, whereas for a PGA of  $5 \text{ m/s}^2$ , the standard deviation is 0.17. We  
853 also found that, whatever the soil profiles used (among the 3 soil profiles considered), the  
854 overall code-to-code variability in the worst case (with strain levels exceeding 1%) remained  
855 lower than the random variability of GMPE single-station  $\sigma$  values for PGA. Nevertheless, an  
856 important conclusion is that given the scatter in the nonlinear results, a realistic analysis  
857 should use more than one code to perform a site response computation.

858 The effect of different non-linear soil model implementations was explored in this study and  
859 our main observations indicate that the epistemic uncertainty (i.e. the code-to-code  
860 variability) can be significantly reduced by describing more precisely some specific input  
861 parameters, especially the soil shear strength profile, which is found to be a key specification  
862 in addition to the degradation curves. In addition, when damping control is used, the  
863 variability of the stress-strain curves was found to be large. This point deserves further  
864 research in future studies. All these features and conclusions need to be checked against  
865 actual data to provide support for defining best practice for modeling non-linearities in soft

866 soils. In that aim, vertical arrays having multiple down-hole sensors constitute indeed the best  
867 available in-situ instrumentation to go forward with this kind of study. The benchmark  
868 undoubtedly benefits a lot from the various expertise fields of the participants ranging from  
869 geotechnical earthquake engineering to engineering seismology.

## 870 **Data and resources**

871 Time histories used in this study were collected from the KiK-net web site  
872 [www.kik.bosai.go.jp](http://www.kik.bosai.go.jp) and <http://www.kik.bosai.go.jp/kik/> (last accessed November 2011) and  
873 from University of Iceland, Engineering Research Institute, Applied Mechanics Laboratory,  
874 Reykjavik, Iceland.

875 Some codes used in this work have URL links:

876 ASTER: <http://www.code-aster.org>;

877 EPISPEC1D: <http://efispec.free.fr>;

878 real ESSI Simulator : [http://sokocalo.engr.ucdavis.edu/~Jeremić/Real\\_ESSI\\_Simulator/](http://sokocalo.engr.ucdavis.edu/~Jeremić/Real_ESSI_Simulator/);

879 Opensees: <http://opensees.berkeley.edu/>

880 DEEPSOIL: <http://deepsoil.cce.illinois.edu/>

881 SeismoSoil: <http://asimaki.caltech.edu/resources/index.html#software>

## 882 **Acknowledgements**

883 Such an exercise was made possible by the interest and funding of the French and Italian  
884 nuclear industry under the project "SIGMA". It was made successful thanks to the dedicated  
885 and proactive participation of many teams from all over the world: A large number of teams

886 reacted very positively to our invitation to take part in this (risky) benchmarking exercise,  
887 among them the developers of a wide variety of internationally used constitutive laws and/or  
888 codes. Such a broad participation witnesses the actual need for such a carefully controlled  
889 comparison, and also brought an invaluable enrichment to the project, which undoubtedly  
890 benefitted greatly from the deep expertise of the participants. PRENOLIN is part of two larger  
891 projects: SINAPS@, supported from French funding managed by the National Research  
892 Agency under the program “Future Investments” (SINAPS@ reference No. ANR-11-RSNR-  
893 0022), and SIGMA, funded by a consortium of nuclear operators (EDF, CEA, AREVA,  
894 ENL).

895

896

## 897 **References**

- 898 Aki, K., Richards, P.G., 2002. Quantitative seismology.
- 899 Aubry, D., Hujeux, J.C., Lassoudiere, F., Meimon, Y., 1982. A double memory model with  
900 multiple mechanisms for cyclic soil behaviour, in: Proceedings of the Int. Symp. Num. Mod.  
901 Geomech. pp. 3–13.
- 902 Aubry, D., Modaressi, A., 1996. GEFDYN, Manuel scientifique. Éc. Cent. Paris LMSS-Mat.
- 903 Bardet, J.P., Ichii, K., Lin, C.H., 2000. EERA: a computer program for equivalent-linear  
904 earthquake site response analyses of layered soil deposits. University of Southern California,  
905 Department of Civil Engineering.
- 906 Benz, T., 2006. Small strain stiffness of soils and its consequences. Dr. Thesis IGS Univ.  
907 Stuttg.
- 908 Benz, T., Vermeer, P.A., Schwab, R., 2009. A small-strain overlay model. Int. J. Numer.  
909 Anal. Methods Geomech. 33, 25–44.
- 910 Beresnev, I.A., Wen, K.-L., Yeh, Y.T., 1995. Nonlinear Soil Amplification: Its Corroboration  
911 in Taiwan. Bull. Seismol. Soc. Am. 85, 456–515.
- 912 Biot, M.A., 1956. Theory of Propagation of Elastic Waves in a Fluid-Saturated Porous Solid.  
913 I. Low-Frequency Range. J. Acoust. Soc. Am. 28, 168–178. doi:10.1121/1.1908239
- 914 Blanch, J.O., Robertsson, J.O., Symes, W.W., 1995. Modeling of a constant Q: Methodology  
915 and algorithm for an efficient and optimally inexpensive viscoelastic technique. Geophysics  
916 60, 176–184.
- 917 Bonilla, L.F., Archuleta, R.J., Lavallée, D., 2005. Hysteretic and Dilatant Behavior of  
918 Cohesionless Soils and Their Effects on Nonlinear Site Response: Field Data Observations  
919 and Modeling. Bull. Seismol. Soc. Am. 95, 2373–2395.
- 920 Boore, D.M., Bommer, J.J., 2005. Processing of strong-motion accelerograms: needs, options

921 and consequences. *Soil Dyn. Earthq. Eng.* 25, 93–115.

922 Cundall, P., 2006. A simple hysteretic damping formulation for dynamic continuum  
923 simulations, in: *Proceedings of the 4th International FLAC Symposium on Numerical  
924 Modeling in Geomechanics*. Minneapolis: Itasca Consulting Group.

925 Dafalias, Y.F., Manzari, M.T., 2004. Simple plasticity sand model accounting for fabric  
926 change effects. *J. Eng. Mech.* 130, 622–634.

927 Darendeli, M.B., 2001. Development of a new family of normalized modulus reduction and  
928 material damping curves.

929 Day, S.M., Bradley, C.R., 2001. Memory-efficient simulation of anelastic wave propagation.  
930 *Bull. Seismol. Soc. Am.* 91, 520–531.

931 Day, S.M., Minster, J.B., 1984. Numerical simulation of attenuated wavefields using a Padé  
932 approximant method. *Geophys. J. Int.* 78, 105–118.

933 Derras, B., Bard, P.-Y., Cotton, F., Bekkouche, A., 2012. Adapting the Neural Network  
934 Approach to PGA Prediction: An Example Based on the KiK-net Data. *Bull. Seismol. Soc.  
935 Am.* 102, 1446–1461.

936 Elgamal, A., Yang, Z., Parra, E., Ragheb, A., 2003. Modeling of cyclic mobility in saturated  
937 cohesionless soils. *Int. J. Plast.* 19, 883 – 905. doi:[http://dx.doi.org/10.1016/S0749-  
938 6419\(02\)00010-4](http://dx.doi.org/10.1016/S0749-6419(02)00010-4)

939 Foerster, E., Gélis, C., De Martin, F., Bonilla, L.-F., 2015. Numerical study of 1D/2D wave  
940 propagation in the <sup>[P]</sup><sub>SEP</sub> Mygnodian basin, EUROSEISTEST, Northern Greece. 9ème Colloq.  
941 AFPS.

942 Gerolymos, N., Gazetas, G., 2006. Winkler model for lateral response of rigid caisson  
943 foundations in linear soil. *Soil Dyn. Earthq. Eng.* 26, 347–361.

944 Gerolymos, N., Gazetas, G., 2005. Constitutive model for 1-D cyclic soil behaviour applied to  
945 seismic analysis of layered deposits. *Soils Found.* 45, 147–159.

946 Graves, R.W., Day, S.M., 2003. Stability and accuracy analysis of coarse-grain viscoelastic  
947 simulations. *Bull. Seismol. Soc. Am.* 93, 283–300.

948 Hashash, Y.M.A., Groholski, D.R., Phillips, C.A., Park, D., Musgrove, M., 2012. DEEPSOIL  
949 5.1. User Man. Tutor. 107.

950 Haskell, N.H., 1953. The dispersion of surface waves in multilayered media. *Bull. Seismol.*  
951 *Soc. Am.* 43, 17–34.

952 IAI, S., MATSUNAGA, Y., KAMEOKA, T., 1992. Strain space plasticity model for cyclic  
953 mobility. *SOILS Found.* 32, 1–15. doi:10.3208/sandf1972.32.2\_1

954 Iai, S., Morita, T., Kameoka, T., Matsungaya, Y., Abiko, K., 1995. Response of a dense sand  
955 deposit during 1993 Kushiro-Oki earthquake. *Soils Found.* 35, 115–131.

956 Iai, S., Ozutsumi, O., 2005. Yield and cyclic behaviour of a strain space multiple mechanism  
957 model for granular materials. *Int. J. Numer. Anal. Methods Geomech.* 29, 417–442.  
958 doi:10.1002/nag.420

959 Iai, S., Tobita, T., Ozutsumi, O., Ueda, K., 2011. Dilatancy of granular materials in a strain  
960 space multiple mechanism model. *Int. J. Numer. Anal. Methods Geomech.* 35, 360–392.  
961 doi:10.1002/nag.899

962 Ishibashi, I., Zhang, X., 1993. Unified Dynamic shear moduli and damping ratio of sand and  
963 clay. *Soils Found.* 33, 182–191.

964 Ishihara, K., 1996. *Soil Behaviour in Earthquake Geotechnics*. Clarenton Press, Oxford.

965 ITASCA, F., 2011. 7.0: User Manual. Licence Number 213-039-0127-18973. Sapienza—  
966 Univ Rome Earth Sci. Dep.

967 Iwan, W.D., 1967. On a class of models for the yielding behavior of continuous and  
968 composite systems. *J. Appl. Mech.* 34, 612–617.

969 Johnston, D.H., Toksoz, M.N., Timur, A., 1979. Attenuation of seismic waves in dry and  
970 saturated rocks; II, Mechanisms. *Geophysics* 44, 691–711. doi:10.1190/1.1440970

971 Kontoe, S., 2006. Development of time integration schemes and advanced boundary  
972 conditions for dynamic geotechnical analysis. Imperial College London (University of  
973 London).

974 Kwok, A.O., Stewart, J.P., Hashash, Y.M., 2008. Nonlinear ground-response analysis of  
975 Turkey Flat shallow stiff-soil site to strong ground motion. *Bull. Seismol. Soc. Am.* 98, 331–  
976 343.

977 Leurer, K.C., 1997. Attenuation in fine-grained marine sediments; extension of the Biot-Stoll  
978 model by the “effective grain model” (EGM). *Geophysics* 62, 1465–1479.  
979 doi:10.1190/1.1444250

980 Liu, P., Archuleta, R.J., 2006. Efficient Modeling of Q for 3D Numerical Simulation of Wave  
981 Propagation. *Bull. Seismol. Soc. Am.* 96, 1352–1358. doi:10.1785/0120050173

982 Li, W., Assimaki, D., 2010. Site-and motion-dependent parametric uncertainty of site-  
983 response analyses in earthquake simulations. *Bull. Seismol. Soc. Am.* 100, 954–968.

984 Matasović, N., Ordóñez, G., 2007. D-MOD2000. GeoMotions, LLC, Computer Software.

985 Matasovic, N., vucetic, M., 1995. Generalized cyclic-degradation-pore-pressure generation  
986 model for clays. *J. Geotech. Eng.* 121, 33–43.

987 Matasovic, N., vucetic, M., 1993. Analysis of seismic records obtained on november 24, 1987  
988 at the Wildlife liquefaction array. University of California, Los Angeles.

989 Mercerat, E.D., Glinsky, N., 2015. A nodal discontinuous Galerkin method for non-linear soil  
990 dynamics. 6th Int. Conf. Earthq. Geotech. Eng.

991 Moczo, P., Kristek, J., Gális, M., 2004. Simulation of the planar free surface with near-  
992 surface lateral discontinuities in the finite-difference modeling of seismic motion. *Bull.*  
993 *Seismol. Soc. Am.* 94, 760–768.

994 Modaressi, H., Foerster, E., 2000. CyberQuake. User’s Man. BRGM Fr.

995 Olsen, K., Day, S., Bradley, C., 2003. Estimation of Q for long-period (> 2 sec) waves in the

996 Los Angeles basin. *Bull. Seismol. Soc. Am.* 93, 627–638.

997 Peyrusse, F., Glinsky, N., Gélis, C., Lanteri, S., 2014. A high-order discontinuous Galerkin  
998 method for viscoelastic wave propagation, in: *Spectral and High Order Methods for Partial*  
999 *Differential Equations-ICOSAHOM 2012*. Springer, pp. 361–371.

1000 Phillips, C., Hashash, Y.M.A., 2009. Damping formulation for nonlinear 1D site response  
1001 analyses. *Soil Dyn. Earthq. Eng.* 29, 1143 – 1158.  
1002 doi:<http://dx.doi.org/10.1016/j.soildyn.2009.01.004>

1003 Pisanò, F., Jeremić, B., 2014. Simulating stiffness degradation and damping in soils via a  
1004 simple visco-elastic–plastic model. *Soil Dyn. Earthq. Eng.* 63, 98–109.

1005 Potts, D.M., Zdravkovic, L., 1999. *Finite element analysis in geotechnical engineering:*  
1006 *theory*. Imperial College of Science, Technology and Medicine. Thomas Telford Publishing,  
1007 Thomas Telford Ltd, ISBN 0-7277-2783-4.

1008 Puzrin, A.M., Shiran, A., 2000. Effects of the constitutive relationship on seismic response of  
1009 soils. Part I. Constitutive modeling of cyclic behavior of soils. *Soil Dyn. Earthq. Eng.* 19, 305  
1010 – 318. doi:[http://dx.doi.org/10.1016/S0267-7261\(00\)00027-0](http://dx.doi.org/10.1016/S0267-7261(00)00027-0)

1011 Régnier, J., Cadet, H., Bonilla, L., Bertand, E., Semblat, J.F., 2013. Assessing nonlinear  
1012 behavior of soil in seismic site response: Statistical analysis on KiK-net strong motion data.  
1013 *Bull. Seismol. Soc. Am.* 103, 1750–1770.

1014 Rodriguez-Marek, A., Mantalva, G. 1, Cotton, F., Bonilla, F., 2011. Analysis of Single-  
1015 Station Standard Deviation Using the KiK-net Data. *Bull. Seismol. Soc. Am.* 101, 1242–  
1016 1258.

1017 Sandıkkaya, M.A., Akkar, S., Bard, P.-Y., 2013. A Nonlinear Site-Amplification Model for  
1018 the Next Pan-European Ground-Motion Prediction Equations. *Bull. Seismol. Soc. Am.* 103,  
1019 19–32.

1020 Santisi d'Avila, M.P., Lenti, L., Semblat, J.-F., 2012. Modelling strong seismic ground



1021 motion: three-dimensional loading path versus wavefield polarization. *Geophys. J. Int.* 190,  
1022 1607–1624.

1023 Santisi d’Avila, M.P., Semblat, J.-F., 2014. Nonlinear seismic response for the 2011 Tohoku  
1024 earthquake: borehole records versus one-directional three-component propagation models.  
1025 *Geophys. J. Int.* 197, 566–580.

1026 Santisi d’Avila, M.P., Semblat, J.-F., Lenti, L., 2013. Strong Ground Motion in the 2011  
1027 Tohoku Earthquake: A One-Directional Three-Component Modeling. *Bull. Seismol. Soc.*  
1028 *Am.* 103, 1394–1410.

1029 Schanz, T., Vermeer, P.A., Bonnier, P.G., 1999. The hardening soil model: formulation and  
1030 verification. *2000 Comput. Geotech.* 281–296.

1031 Schnabel, P.B., Lysmer, J., Seed, H.B., 1972. SHAKE : a computer program for earthquake  
1032 response analysis of horizontally layered sites (report). Earthquake Engineering Research  
1033 Centre, Berkeley, California.

1034 Seed, H., 1969. I. M. Idriss, Influence of soil conditions on ground motions during  
1035 earthquakes, *J. Soil Mech Found Div Amer Soc Civ Eng* 95.

1036 Semblat, J.F., 1997. Rheological Interpretation of Rayleigh Damping. *J. Sound Vib.* 206,  
1037 741–744. doi:10.1006/jsvi.1997.1067

1038 Shi, J., Asimaki, D., 2016. From stiffness to strength: Formulation and validation of a hybrid  
1039 hyperbolic nonlinear soil model for site response analyses. *Bull. Seismol. Soc. Am.*

1040 Stewart, J., Kwok, A., 2009. Nonlinear Seismic Ground Response Analysis: Protocols and  
1041 Verification Against Array Data. *PEER Annu. Meet. San Franc.-Present.* 84.

1042 Susumu Iai, T.K., Yoasuo Matsunaga, 1990. Strain space plasticity model for cyclic mobility  
1043 (No. 4). port and harbour reasearch insitute.

1044 Taborda, D.M., Zdravkovic, L., Kontoe, L., Potts, D.M., 2010. Alternative formulations for  
1045 cyclic nonlinear models: parametric study and comparative analyses. *Numer. Methods*

1046 Geotech. Eng. NUMGE 2010 Benz Nord. Eds CRC Press, 423–428.

1047 Thomson, W.T., 1950. Transmission of elastic waves through a stratified solid. *J. Appl. Phys.*

1048 21, 89–93.

1049 Tropeano, G., Chiaradonna, A., onofrio, A. d', Sivistri, F., 2015. An innovative computer

1050 code for 1D seismic response analysis including shear strength of soils. 101680geotSIP 15-P-

1051 017.

1052 Vucetic, M., Dobry, R., 1991. Effect of soil plasticity on cyclic response. *J. Geotech. Eng.*

1053 117.

1054 Yang, Z., Elgamal, A., Parra, E., 2003. Computational model for cyclic mobility and

1055 associated shear deformation. *J. Geotech. Geoenvironmental Eng.* 129, 1119–1127.

1056 Yu, G., Anderson, J.G., Siddharthan, R.A.J., 1993. On the characteristics of nonlinear soil

1057 response. *Bull. Seismol. Soc. Am.* 83, 218–244.

1058 Zeghal, M., Elgamal, A.-W., Tang, H.T., Srepp, J.C., 1995. Lotung downhole array. II:

1059 Evaluation of soil nonlinear properties. *J. Geotech. Eng.* 121, 363–378.

1060

1061

1062 Mailing address:

1063

- 1064 • Julie Régnier, CEREMA, DTer Méditerranée, 56 Bd Stalingrad 06300 Nice, France

- 1065 • Luis-Fabian Bonilla, IFSTTAR, 14-20 Boulevard Newton - Champs-sur-Marne - 77447

1066 Marne-la-Vallée Cedex 2, France

- 1067 • Pierre-Yves Bard, IFSTTAR and Université Grenoble Alpes ISTERre, CS 40700, 38058

1068 GRENOBLE Cedex 9, France

- 1069 • Etienne Bertrand, CEREMA, DTer Méditerranée, 56 Bd Stalingrad 06300 Nice, France

- 1070 • Fabrice Hollender, CEA, DEN, 13108 St Paul lez Durance, France

- 1071 • Hiroshi Kawase, DPRI, Gokasho,Uji,Kyoto 611-0011 Japan

- 1072 • Deborah Sicilia, EDF - DPI-CEIDRE, TEGG, 905 av du Camp Menthe,13097 Aix-en-

1073 Provence Cedex 2, France

- 1074 • Pedro Arduino, Department of Civil & Environmental Engineering, University of Washington,

1075 Seattle, WA, USA

- 1076 • Angelo Amorosi, Sapienza, University of Rome, Via Eudossiana, 18 - 00184 Roma, Italy

- 1077 • Domniki Asimaki, California Institute of Technology, Campus Address: 1200 E California

1078 blvd, Pasadena CA 91125, US

- 1079 • Daniela Boldini, University of Bologna, Dipartimento di Ingegneria Civile, Chimica,

1080 Ambientale e dei Materiali , Via Terracini 28, Bologna, Italy

- 1081 • Long Chen, Department of Civil & Environmental Engineering, University of Washington,

1082 Seattle, WA, USA

- 1083 • Anna Chiaradonna, Department of Civil, Architectural and Environmental Engineering,

1084 Federico II University, via Claudio, 21 80125 Naples, Italy.

- 1085 • Florent DeMartin, BRGM (French Geological Survey), Direction of Risks and Prevention, 3  
1086 Avenue Claude Guillemin, 45100 Orléans, France
- 1087 • Marco Ebrille, Geodata, Corso Bolzano, 14 - 10121 Torino, Italy
- 1088 • Ahmed Elgamal, University of California, San Diego, Dept. of Structural Engineering, La  
1089 Jolla, CA 92093-0085, USA
- 1090 • Gaetano Falcone, Politecnico of Bari, Via Amendola 126, Bari, Italy
- 1091 • Evelyne Foerster, CEA, DEN/DM2S/SEMT/EMSI and SEISM Institute Paris-Saclay, 91191  
1092 Gif-sur-Yvette Cedex, France
- 1093 • Sebastiano Foti, Politecnico di Torino, Corso Duca degli Abruzzi, 24 - 10129 Torino, Italy
- 1094 • Evangelia Garini, NTUA National Technical University of Athens, Faculty of Civil  
1095 Engineering , Geotechnical Department, Iroon Polytechniou 9,Zografou 157 80, GREECE
- 1096 • George Gazetas, NTUA National Technical University of Athens, Faculty of Civil  
1097 Engineering , Geotechnical Department, Iroon Polytechniou 9,Zografou 157 80, GREECE
- 1098 • Céline Gélis, IRSN, 31 Avenue de la Division Leclerc, 92260 Fontenay-aux-Roses, France
- 1099 • Alborz Ghofrani, Department of Civil & Environmental Engineering, University of  
1100 Washington, Seattle, WA, USA
- 1101 • Amalia Giannakou, Fugro Sial, Esentepe mah. Yazarlar sok. No.16 34394 Gayrettepe, Şişli-  
1102 İstanbul / Turkey
- 1103 • James R. Gingery, 9500 Gilman Dr 92093 La Jolla Californie Etats-Unis,US.
- 1104 • Nathalie Glinsky, CEREMA, DTer Méditerranée, 56 Bd Stalingrad 06300 Nice, France
- 1105 • Joseph Harmon, University of Illinois at Urbana-Champaign, 2230c Newmark Lab, 205 N  
1106 Mathews, M/C 250, Urbana, IL 61801 , US

- 1107 • Youssef Hashash, University of Illinois at Urbana-Champaign, 2230c Newmark Lab, 205 N  
1108 Mathews, M/C 250, Urbana, IL 61801 , US
- 1109 • Susumu Iai, DPRI, Gokasho,Uji,Kyoto 611-0011 Japan
- 1110 • Boris Jeremić, CEED, University of California, Davis California 95616, USA. And  
1111 EESA, Lawrence Berkeley National Laboratory, Berkeley, CA 94720 USA
- 1112 • Steve Kramer, 132 I More Hall, Department of Civil & Environmental Engineering,  
1113 University of Washington, Seattle, WA, 98195-2700, US
- 1114 • Stavroula Kontoe, Imperial College, South Kensington Campus, London SW7 2AZ, UK.
- 1115 • Jozef Kristek, Comenius University Bratislava Faculty of Mathematics, Physics and  
1116 Informatics Mlynská dolina F1 84248 Bratislava, Slovakia.
- 1117 • Giuseppe Lanzo, Sapienza University of Rome, Via A. Gramsci 53, 00197 Rome, Italy
- 1118 • Annamaria di Lernia, Politecnico of Bari, Via Amendola 126, Bari, Italy Italy
- 1119 • Fernando Lopez-Caballero, CentraleSupélec, Paris-Saclay University, MSS-Mat CNRS UMR  
1120 8579, Grande Voie des Vignes, Châtenay-Malabry 92290, France
- 1121 • Marianne Marot, CEREMA, DTer Méditerranée, 56 Bd Stalingrad 06300 Nice, France
- 1122 • Graeme McAllister, Department of Civil Engineering, University of British Columbia,  
1123 Vancouver, BC, Canada.
- 1124 • E. Diego Mercerat, CEREMA, DTer Méditerranée, 56 Bd Stalingrad 06300 Nice, France
- 1125 • Peter Moczó Comenius University Bratislava Faculty of Mathematics, Physics and  
1126 Informatics Mlynská dolina F1 84248 Bratislava, Slovakia.
- 1127 • Silvana Montoya-Noguera, CentraleSupélec, Paris-Saclay University, MSS-Mat CNRS UMR  
1128 8579, Grande Voie des Vignes, Châtenay-Malabry 92290, France

- 1129 • Michael Musgrove, University of Illinois at Urbana-Champaign, 2230c Newmark Lab, 205 N  
1130 Mathews, M/C 250, Urbana, IL 61801 , US
- 1131 • Alex Nieto-Ferro, Dépt. Analyses en Mécanique Avancée, EDF Lab Paris-Saclay, 7 boulevard  
1132 Gaspard Monge, 91120 PALAISEAU
- 1133 • Alessandro Pagliaroli, University of Chieti-Pescara, viale Pindaro 42, 65129 Pescara, Italy.
- 1134 • Federico Pisanò, Delft University of Technology, Stevinweg 1, 2628 CN Delft, The  
1135 Netherlands
- 1136 • Aneta Richterova, Comenius University Bratislava Faculty of Mathematics, Physics and  
1137 Informatics Mlynská dolina F1 84248 Bratislava, Slovakia.
- 1138 • Suwal Sajana, Sapienza University of Rome, Via A. Gramsci 53, 00197 Rome, Italy
- 1139 • Maria Paola Santisi d'Avila, UNS, Nice, Campus Valrose, 28 avenue Valrose, 06108 Nice  
1140 cedex 2, France
- 1141 • Jian Shi, California Institute of Technology, Campus Address: 1200 E California blvd,  
1142 Pasadena CA 91125, US
- 1143 • Francesco Silvestri, Department of Civil, Architectural and Environmental Engineering,  
1144 University of Napoli Federico II, via Claudio 21, 80125 Napoli, Italy.
- 1145 • Mahdi Taiebat: Department of Civil Engineering, University of British Columbia, Vancouver,  
1146 BC, Canada
- 1147 • Giuseppe Tropeano, Department of Civil, Environmental Engineering and Architecture,  
1148 University of Cagliari, Piazza d'Armi 09123, Cagliari, Italy.
- 1149 • Luca Verrucci, Dipartimento di Ingegneria Strutturale e Geotecnica, University of Rome, via  
1150 Eudossiana 18, 00184, Rome, Italy.

1151 • Kohei Watanabe, Shimizu Corporation, No. 16-1, Kyobashi 2-chome, Chuo-ku, Tokyo 104-  
1152 8370, Japan

1153

1154

1155 **TABLES**

1156 *Table 1: Soil properties for all three simple profile cases studied here (P1-3), for the elastic and non-elastic*  
 1157 *domains.*

Profile	LINEAR									NL <sup>i</sup>
	Z <sup>ii</sup> [m]	V <sub>s</sub> <sup>iii</sup> [m/s]	V <sub>p</sub> <sup>iv</sup> [m/s]	ρ <sup>v</sup> [kg/m <sup>3</sup> ]	Q <sup>vi</sup> Elastic	ξ <sub>min</sub> <sup>vii</sup> Elastic	Q Visco- Elastic	ξ <sub>min</sub> Visco- Elastic	f <sub>0</sub> <sup>viii</sup> Linear Elastic [Hz]	
P1	0-20	300	700	2000	5000	10 <sup>-4</sup>	30	0.0166	3.75	N°1-P1
	-	1000	1900	2500			200	0.0025		-
P2 <i>Mono- layer + V<sub>gradient</sub></i>	0-20	150- 500	360- 1220	2000			34	0.0154 7	1.16	N°1-P2
	20-40						40	0.0250		N°2-P2
	40-60						44	0.0113		N°3-P2
	60-80						47	0.0106		N°4-P2
	80-100						49	0.0102		N°5-P2
	-	2000	3700	2500			200	0.0025		-
P3 <i>Bi-layer</i>	0-20	300	700	2000			30	0.0166	1.48	N°1-P3
	20-100	600	1500	2000			60	0.0083		N°2-P3
	-	2000	3700	2500	200	0.0025	-			

<sup>i</sup> Describe the  $G/G_{max}$  and damping curves used for each soil layer

<sup>ii</sup> Depth of the soil layer

<sup>iii</sup> Shear wave velocity

<sup>iv</sup> Compressional wave velocity

<sup>v</sup> Density

<sup>vi</sup> Quality factor

<sup>vii</sup> Elastic damping

<sup>viii</sup> Fundamental resonance frequency of the soil

1158



1159 *Table 2 Seismic metadata of the two real input motions used in the verification phase of the Prenolin*  
 1160 *project.*

Event Freq. Content	Event ID	Mw <sub>ix</sub>	Z <sup>x</sup> [km]	Epi. Dist. [km]	Station ID	Station Geology	Seismo Comp.	Vs30 <sup>xi</sup> [m/s]
HF	IWTH-170112022202	6.4	122	39	IWTH17 (Kik-net, Japan)	Rock	EW	>1200
LF	06756.20000617	6.6	15	5	Flagbjarnarholt (Iceland)	A	H1	Unknown

1161

<sup>ix</sup> Moment magnitude

<sup>x</sup> Depth of epicenter

<sup>xi</sup> Mean harmonic S-wave velocity over the first 30m depth

1162  
1163

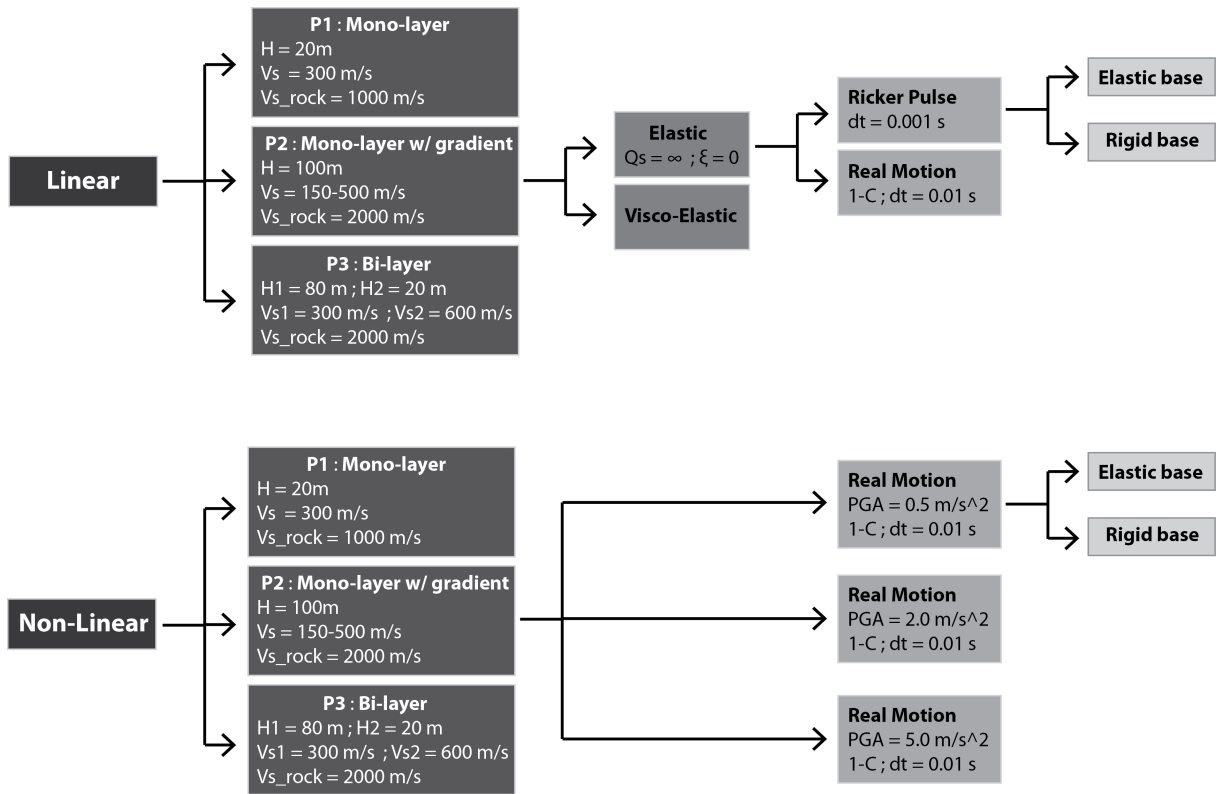
*Table 3: Participants to the PRENOLIN project Verification phase.*

Team Name	Affiliation	Team Index		Code Name	Code Reference
<i>D. Asimaki &amp; J. Shi</i>	<i>Caltech, US</i>	A	0	SeismoSoil	(Shi and Asimaki, 2016; Li and Assimaki, 2010; Matasovic and vucetic, 1993)
<i>S. Iai</i>	<i>DPRI, Kyoto University, Japan</i>	B	0	FLIP	(Iai, 1990)
<i>S. Kramer</i>	<i>Univ. Washington, US</i>	C	0	PSNL	(In development)
<i>E. Foerster</i>	<i>CEA, France</i>	D	0	CYBERQUAKE	(Modaressi and Foerster, 2000)
<i>C. Gelis</i>	<i>IRSN, France</i>	E	0	NOAH-2D	(Iai, 1990)
<i>A. Giannakou</i>	<i>Fugro, France</i>	F	0	DEEPSOIL 5.1	(Hashash et al., 2012)
<i>G. Gazetas, E. Garini &amp; N. Gerolymos</i>	<i>NTUA, Greece</i>	G	0	NL-DYAS	(Gerolymos and Gazetas, 2006, 2005)
<i>J. Gingery &amp; A. Elgamal</i>	<i>UCSD, US</i>	H	0	OPENSEES-UCSD-SOIL-MODEL	See Data and Resources

<i>Y. Hashash &amp; J. Harmon</i>	<i>Univ, Illinois, US</i>	J	0	DEEPSOIL-NL 5.1	(Hashash et al., 2012)
		J	1	DEEPSOIL-EL 5.1	(Hashash et al., 2012)
<i>P. Moczo, J. Kristek &amp; A. Richterova</i>	<i>CUB, Comenius University, Bratislava, Slovakia</i>	K	0	1DFD-NL-IM	
<i>S. Foti &amp; S. Kontoe</i>	<i>Politecnico di Torino &amp; Imperial College, Italy</i>	L	1	ICFEP	(Kontoe, 2006; Potts and Zdravkovic, 1999; Taborda et al., 2010)
		L	2	DEEPSOIL-NL 5.1	(Hashash et al., 2012)
<i>G. Lanzo, S. Suwal, A. Pagliaroli &amp; L. Verrucci</i>	<i>Univ. Rome La Sapienza &amp; University of Chieti-Pescara, Italy</i>	M	0	FLAC_7,00	(ITASCA, 2011)
		M	1	DMOD2000	(Matasović and Ordóñez, 2007)
		M	2	DEEPSOIL 5.1	(Hashash et al., 2012)
<i>F. Lopez-Caballero &amp; S. Montoya-Noguera</i>	<i>ECP, France</i>	N	0	GEFDyn	(Aubry and Modaressi, 1996)
<i>F. De-Martin</i>	<i>BRGM, France</i>	Q	0	EPISPEC1D	(Iai, 1990) See Data and Resources
<i>B. Jeremić, F. Pisanò &amp; K. Watanabe</i>	<i>UCD, LBLN, TU Delft &amp; Shimizu Corp</i>	R	0	real ESSI Simulator	See Data and Resources
<i>A. Nieto-Ferro</i>	<i>EDF, France</i>	S	0	ASTER	See Data and Resources
<i>A. Chiaradonna, F. Silvestri &amp; G. Tropeano</i>	<i>UNICA and Univ. Naples, Italy</i>	T	0	SCOSSA_1,2	(Tropeano et al., 2015)
		T	1	STRATA	
<i>M.P. Santisi d'Avila</i>	<i>Univ. Nice Sophia-Antipolis, France</i>	U	0	SWAP_3C	(Santisi d'Avila et al., 2012, 2013; Santisi d'Avila and Semblat, 2014)
<i>D. Mercerat and N. Glinsky</i>	<i>CEREMA, France</i>	Y	0	DGNL	(Mercerat and Glinsky, 2015)
<i>D. Boldini, A. Amorosi, A. di Lernia &amp; G. Falcone</i>	<i>Univ. Bologna and Sapienza University of Rome, Italy</i>	Z	0	EERA	(Bardet et al., 2000)
		Z	1	PLAXIS	(Benz, 2006; Benz et al., 2009)
<i>M. Taiebat &amp; P. Arduino</i>	<i>UBC, Canada &amp; UW, USA</i>	W	0	Opensees	See Data and Resources

1164

1165

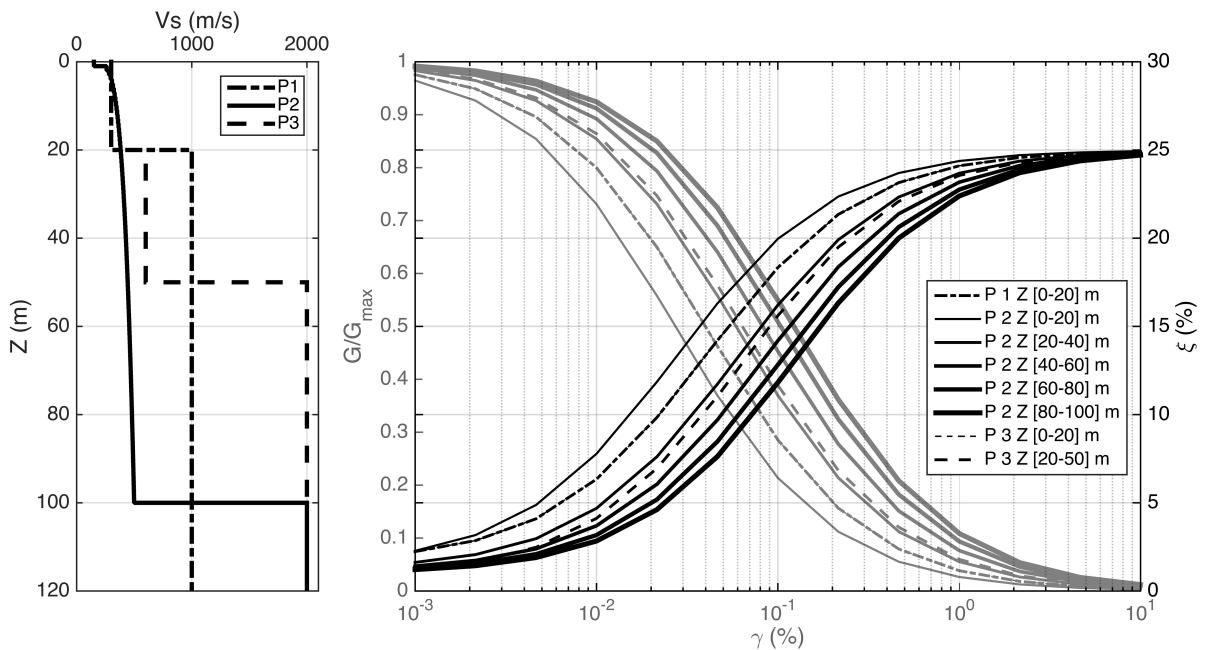


1167

1168 **Figure 1 :** The three simple idealized profile cases studied here (P1-3), for the elastic and non-elastic domains,

1169 and for a rigid and elastic soil-bedrock base, using a Ricker pulse and 3 accelerations of different PGA and

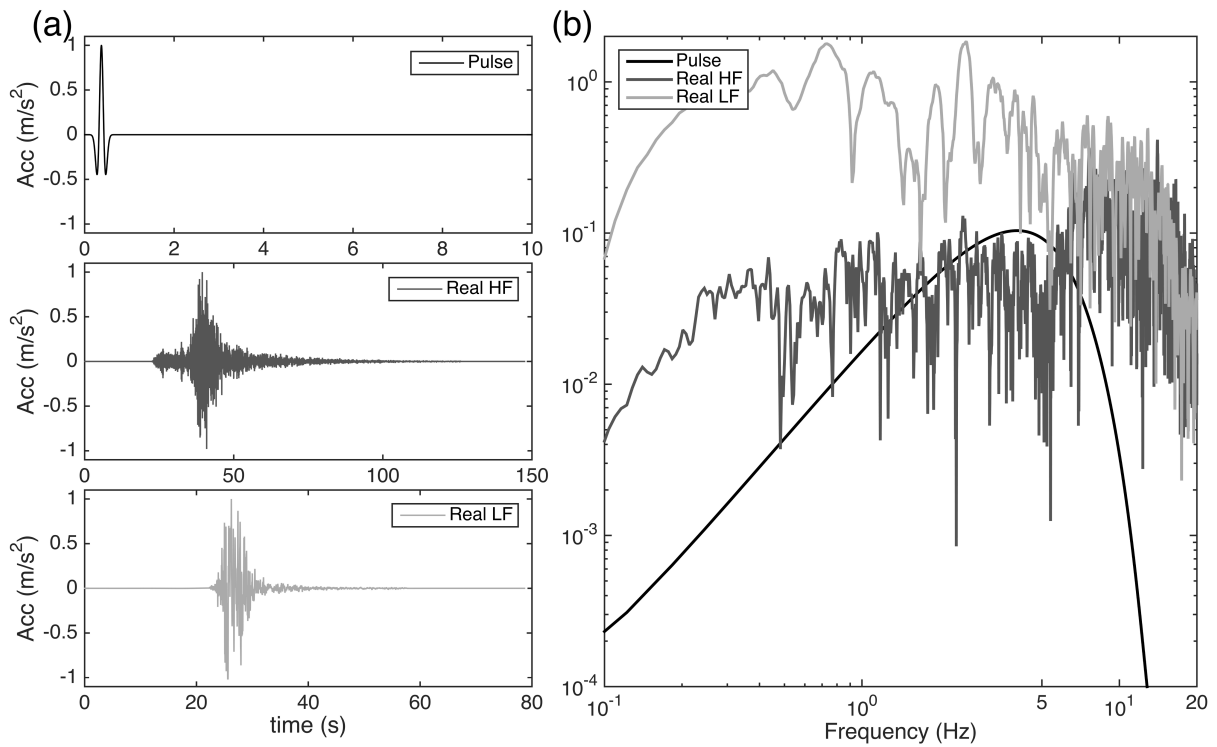
1170 frequency contents.



1171

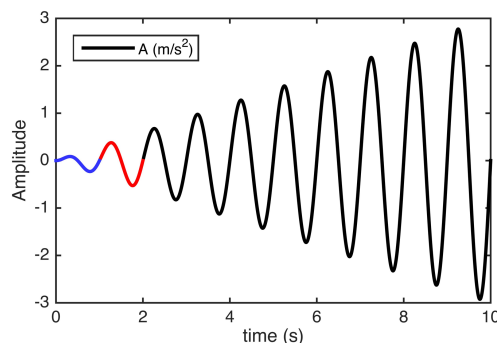
1172

**Figure 2:**  $V_s$  profiles,  $G/G_{max}$  and damping curves for the 3 idealized profiles.



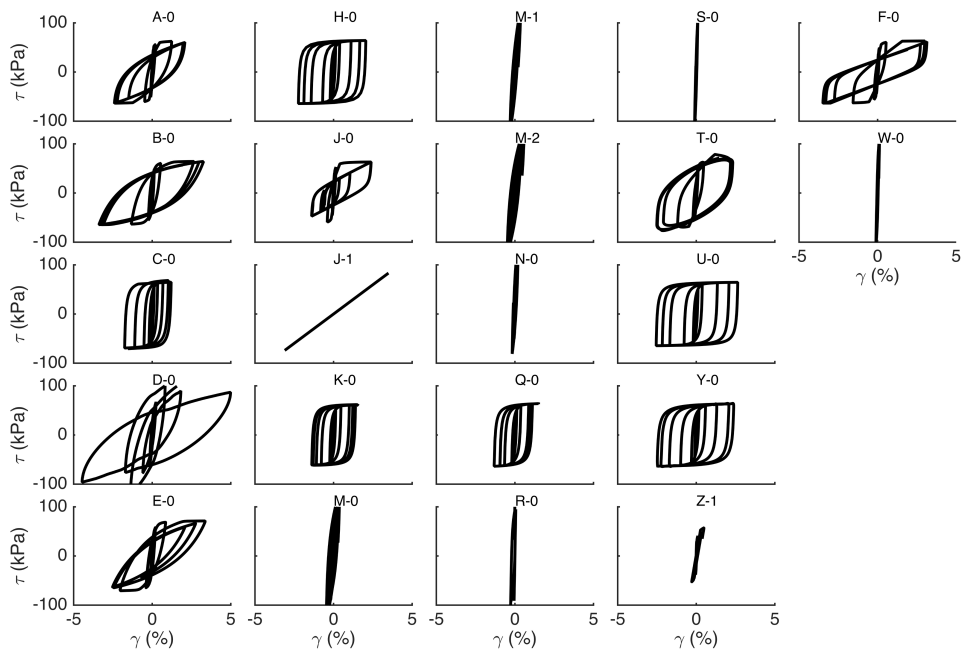
1173

1174 **Figure 3:** Normalized acceleration of the reference motions used for the verification phase (Pulse, real motions  
1175 : High Frequency motion and Low Frequency motion) of this project PRENOLIN (panel a) with the associated  
1176 Fourier spectrum(panel b)



1177

1178 **Figure 4 :** Acceleration time history of the sinusoidal motion with central 1s period



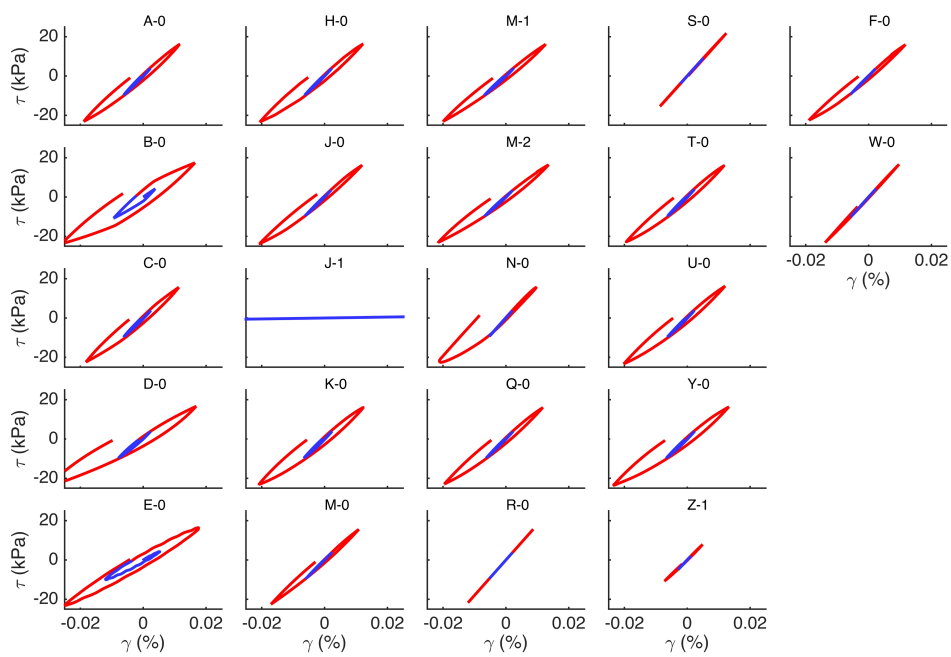
1179

1180 **Figure 5 :** Stress-strain curve for a soil element of shear strength 65kPa subjected to a sinusoidal input seismic

1181

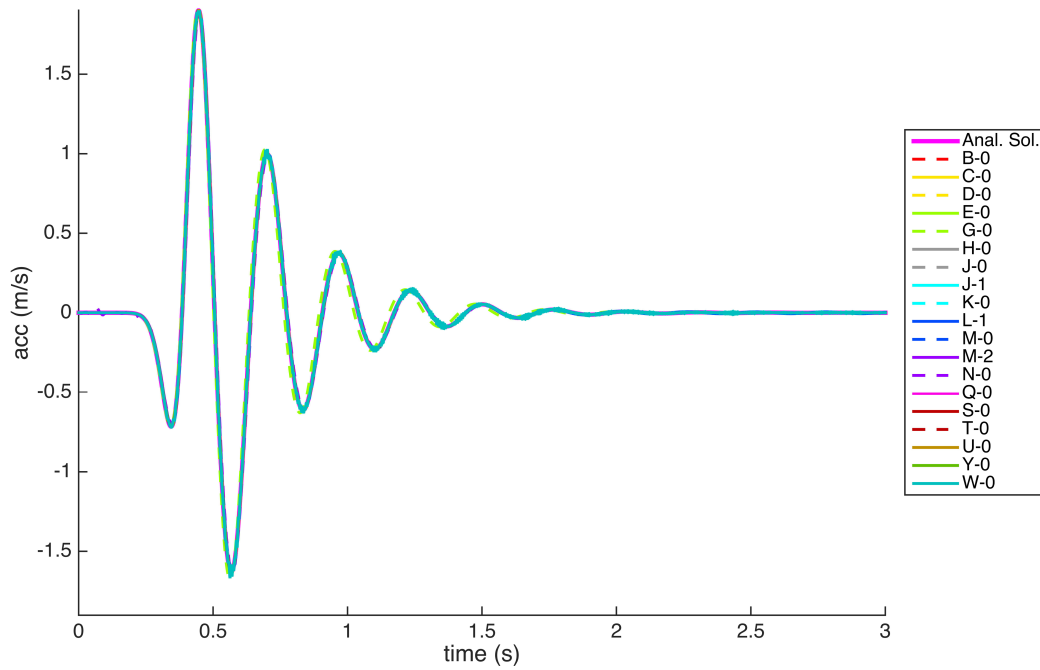
*motion of 10s.*

1182

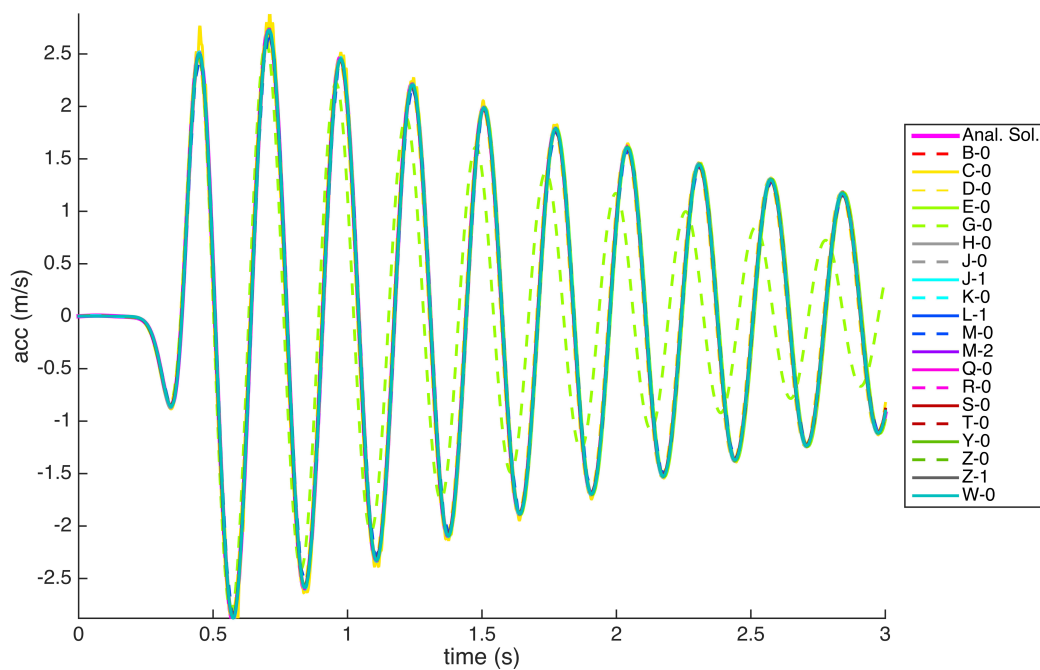


1183

1184 **Figure 6** : Stress-strain curve for a soil element of shear strength 65kPa subjected to the first two cycles of a  
1185 sinusoidal input seismic motion.

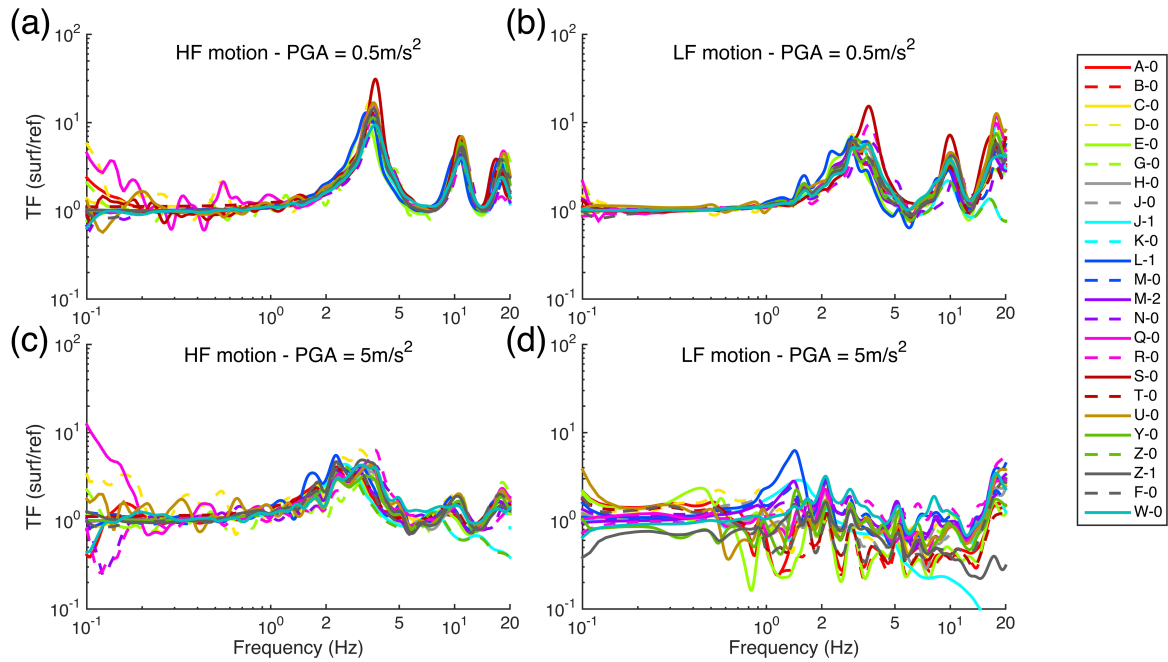


1186  
1187 **Figure 7**: Comparison of the acceleration at the surface of P1 profile, for the pulse-like input motion,  
1188 for the linear elastic computation and for the elastic substratum case.

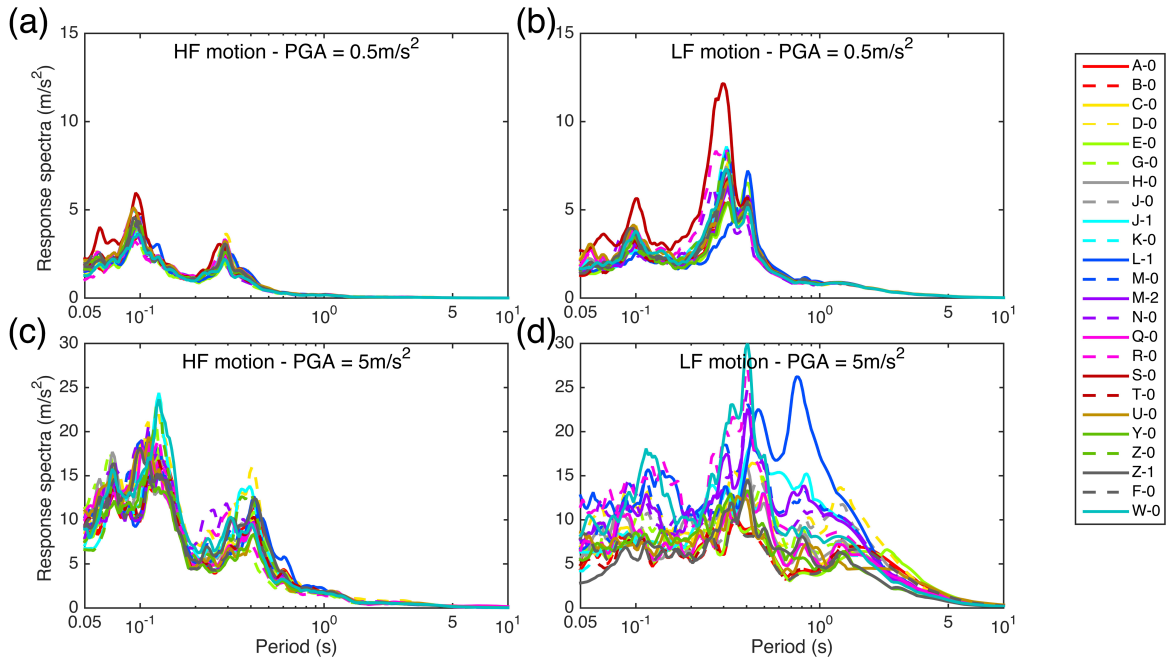


1189  
61

1190 **Figure 8** Comparison of the acceleration at the surface of P1 profile, for the pulse-like input motion,  
 1191 for the linear visco-elastic computation and for the rigid substratum case.



1192  
 1193 **Figure 9** : Comparison of the surface to reference Fourier spectra ratio, for the non-linear computations using  
 1194 the high frequency input motion scaled to 0.5 m/s² (graph a) and scaled at 5m/s² (graph c) and using the low-  
 1195 frequency input motion scaled to 0.5 m/s² (graph b) and scaled at 5m/s² (graph d).



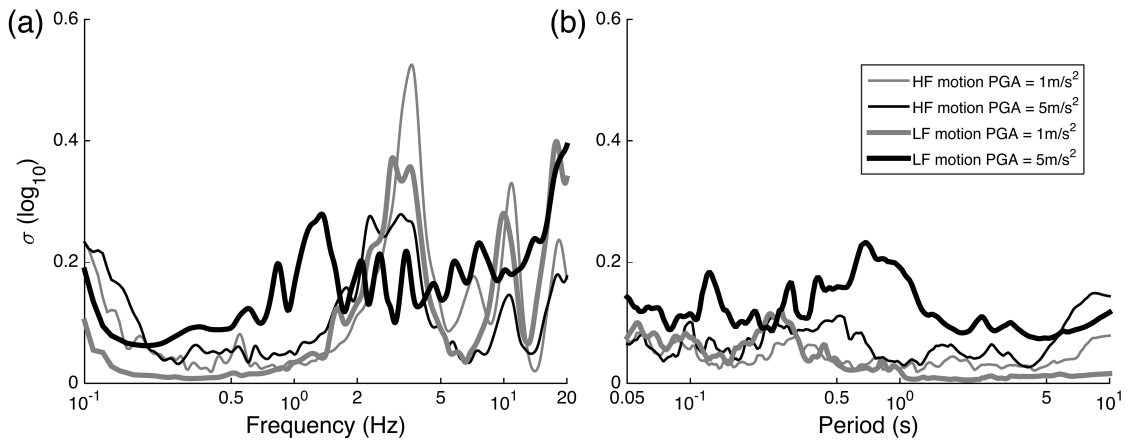
1196

1197

**Figure 10 :** Comparison of the acceleration pseudo-response spectra at the ground surface, for the non-linear computations using the high frequency input motion scaled to  $0.5 \text{ m/s}^2$  (graph a) and scaled at  $5 \text{ m/s}^2$  (graph c) and using the low-frequency input motion scaled to  $0.5 \text{ m/s}^2$  (graph b) and scaled at  $5 \text{ m/s}^2$  (graph d).

1198

1199



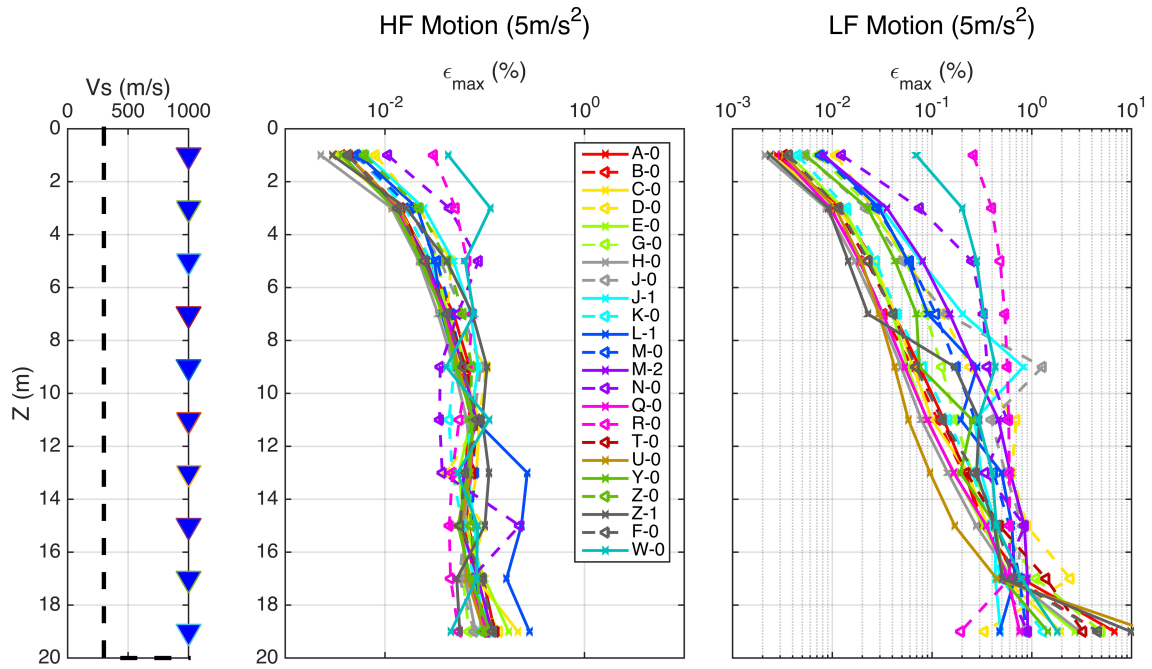
1200

1201

**Figure 11 :** Standard deviation (in log unit) of the transfer function (left) and response spectra (right) depending of the input motion used.

1202



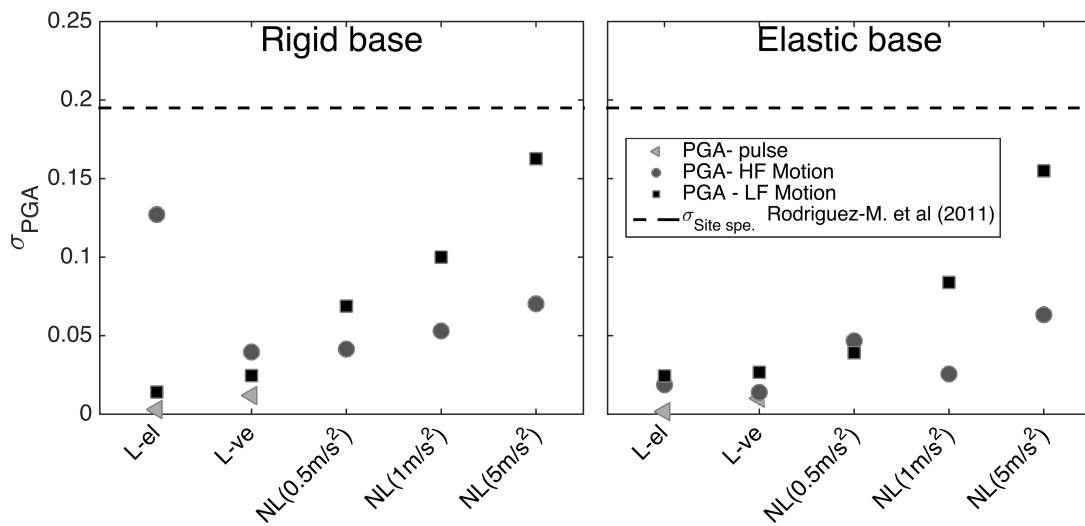


1203

1204

**Figure 12 :** Peak shear strain profiles reached at each depth by each team for the high and low frequency reference motion scaled at the highest PGA level ( $5 \text{ m/s}^2$ ), for the profile 1 and for rigid substratum conditions.

1205



1206

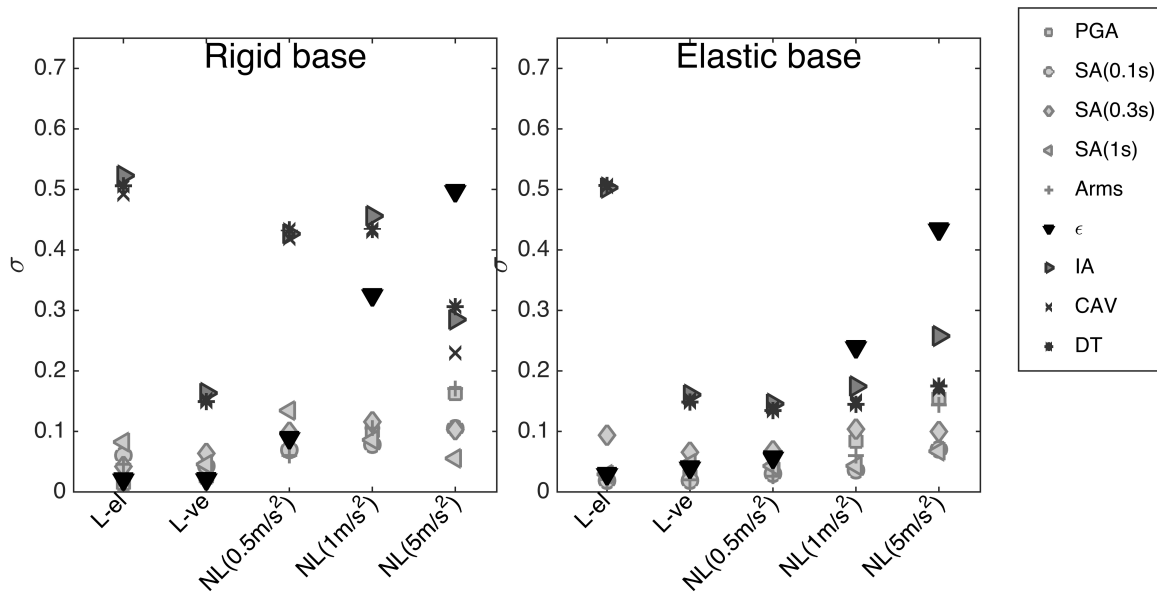
1207

**Figure 13 :** Standard deviation (in log10 unit) of the PGA at the surface of the P1 profile, for the 5 different computational cases (linear –elastic, linear visco-elastic, non-linear with input motion scaled to the lowest ( $0.5 \text{ m/s}^2$ ), medium ( $1 \text{ m/s}^2$ ) and highest ( $5 \text{ m/s}^2$ ) PGA, for the pulse-like, the high frequency and the low frequency content motions. The left sub-plot shows the results for the rigid substratum case and the right sub-plot for the elastic substratum.

1209

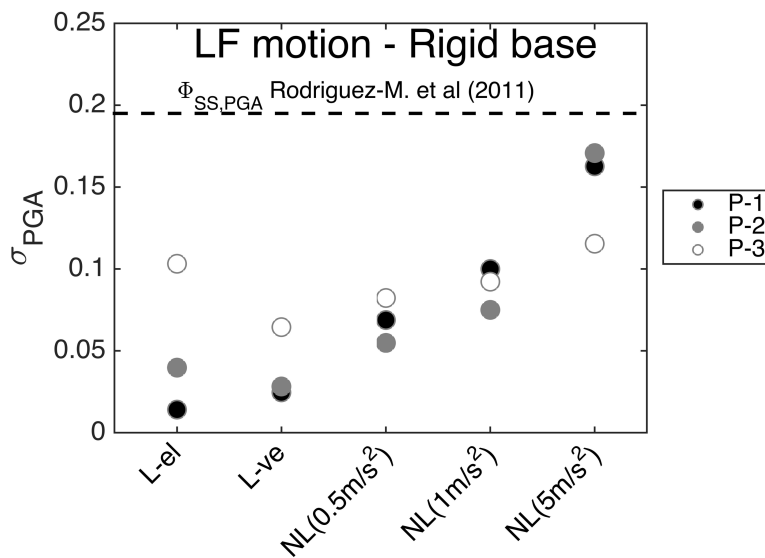
1210

1211



1212

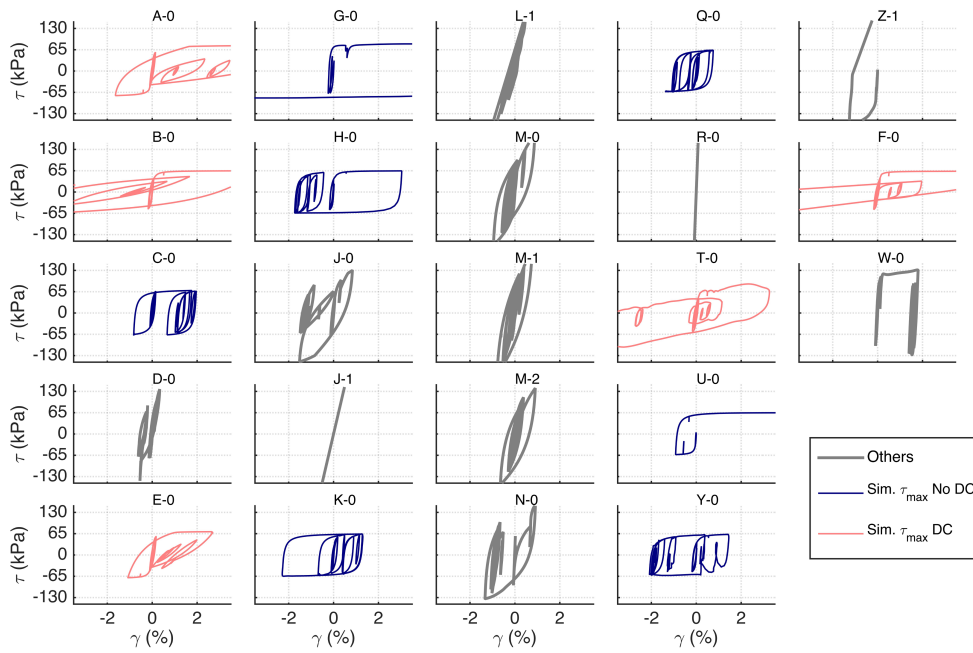
1213 **Figure 14** : Standard deviation (in log unit) of the different intensity parameters for the P1 profile, for the 5  
 1214 different computational cases (linear –elastic, linear visco-elastic, non-linear with input motion scaled to the  
 1215 lowest (0.5m/s<sup>2</sup>), medium (1m/s<sup>2</sup>) and highest (5m/s<sup>2</sup>) PGA, for the low frequency content motion. The left sub-  
 1216 graph shows the results for the rigid substratum case and the right sub-graph for the elastic substratum.



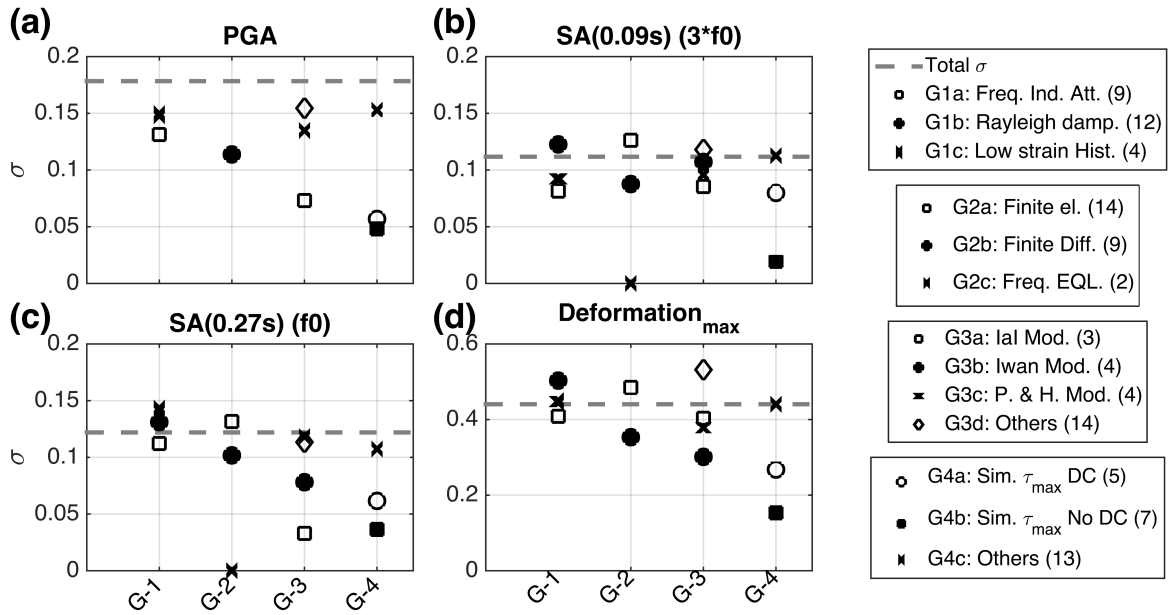
1217

1218 **Figure 15** : Standard deviation (in log unit) of the PGA for the profile 1 2 and 3, for the 5 different  
 1219 computational cases (linear –elastic, linear visco-elastic, non-linear with input motion scaled to the lowest

1220 (0.5m/s<sup>2</sup>), medium (1m/s<sup>2</sup>) and highest (5m/s<sup>2</sup>) PGA, for the low frequency content motion and for the rigid  
 1221 substratum case.



1222  
 1223 **Figure 16** : Stress-strain curves at the bottom of P1 Profile for the Rigid substratum case subjected to the low  
 1224 frequency motion (in color and the high frequency motion in black scaled to the highest PGA (5m/s<sup>2</sup>)). The  
 1225 thicker curves are for code/team couples that exceed the specified shear strength of 65 KPa, whereas the thin  
 1226 curves represent the code/team couples that use 65 KPa. The lighter curves are for codes using damping control  
 1227 and the darker curves the others.



1228

1229

**Figure 17** : Standard deviation values ( $\sigma_{\log}$ , in  $\log_{10}$  units) of four parameters for the non-linear computation

1230

using the low-frequency content input motion scaled to the highest PGA : PGA (a), Response spectra at 0.27 s

1231

(b), Response spectra at 0.09 s (c) all three at the surface of P1 and the maximal shear deformation at the

1232

bottom of the P1 profile (d). The standard deviation are given for each group of the four groupings: depending

1233

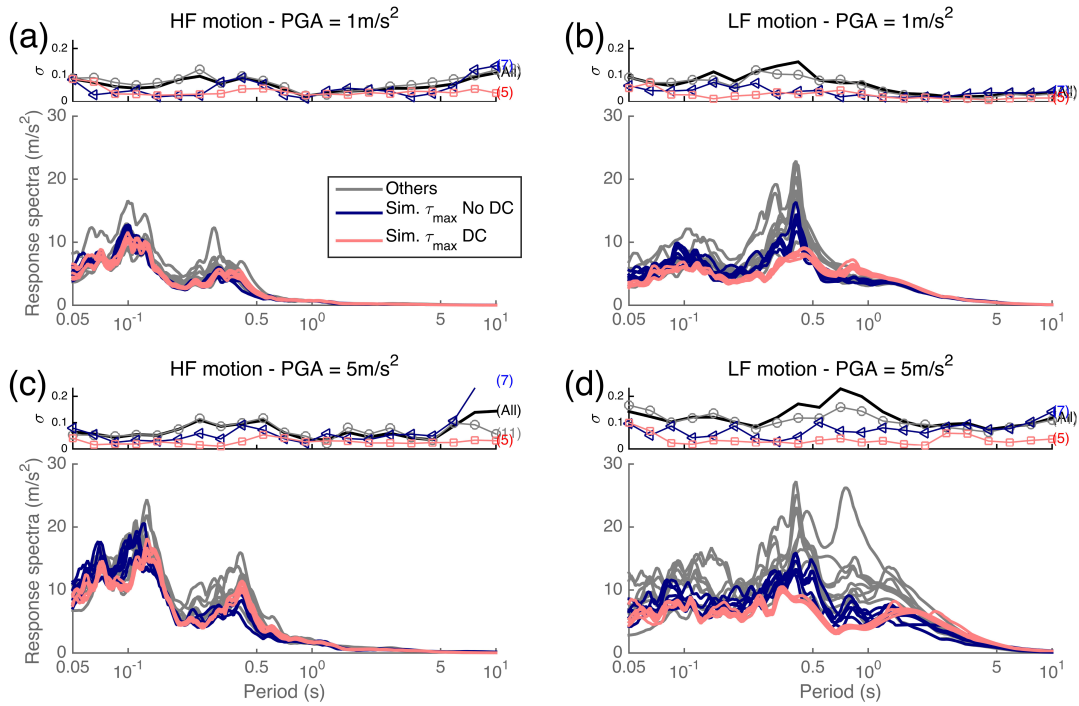
on their low strain attenuation implementation (G-1) their numerical scheme (G-2) their constitutive models (G-

1234

3) and their values of shear strength at the bottom of P1 and use of damping control or not (G-5). The dotted

1235

grey line illustrates the standard deviation for all code/team couples.



1236

1237

**Figure 18** : Comparison of the pseudo- acceleration response spectra at the ground surface of P1 with rigid

1238

substratum condition, for the non-linear computation using for (a) and (c) graphs the high frequency input

1239

motion and for (b) and (d) graphs the low-frequency input motion and with for the (a) and (b) graphs the middle

1240

input motion PGA and the (c) and (d) graphs the highest input motion PGA. The response spectra were sorted

1241

according to three groups: group 1 is composed of the code/team couples using similar  $\tau_{max}$  and damping control

1242

constitutive model. Group 2 use similar  $\tau_{max}$  and no damping control and Group 3 are the other code team

1243

couples. The standard deviation for each sub-group is compared to the standard deviation using all results in

1244

the upper graphs, the figures indicate the number of simulations that are in each group.

1245

1246

## 1247 **List of Figures**

1248 **Figure 1 :** The three simple idealized profile cases studied here (P1-3), for the elastic and non-elastic  
1249 domains, and for a rigid and elastic soil-bedrock base, using a Ricker pulse and 3 accelerations of  
1250 different PGA and frequency contents.

1251 **Figure 2:** Vs profiles,  $G/G_{\max}$  and damping curves for the 3 idealized profiles.

1252 **Figure 3:** Normalized acceleration of the reference motions used for the verification phase (Pulse, real  
1253 motions : High Frequency motion and Low Frequency motion) of this project PRENOLIN (panel a)  
1254 with the associated Fourier spectrum(panel b)

1255 **Figure 4 :** Acceleration time history of the sinusoidal motion with central 1s period

1256 **Figure 5 :** Stress-strain curve for a soil element of shear strength 65kPa subjected to a sinusoidal input  
1257 seismic motion of 10s.

1258 **Figure 6 :** Stress-strain curve for a soil element of shear strength 65kPa subjected to the first two cycles of  
1259 a sinusoidal input seismic motion.

1260 **Figure 7:** Comparison of the acceleration at the surface of P1 profile, for the pulse-like input motion, for  
1261 the linear elastic computation and for the elastic substratum case.

1262 **Figure 8** Comparison of the acceleration at the surface of P1 profile, for the pulse-like input motion, for  
1263 the linear visco-elastic computation and for the rigid substratum case.

1264 **Figure 9 :** Comparison of the surface to reference Fourier spectra ratio, for the non-linear computations  
1265 using the high frequency input motion scaled to  $0.5 \text{ m/s}^2$  (graph a) and scaled at  $5\text{m/s}^2$  (graph c)  
1266 and using the low-frequency input motion scaled to  $0.5 \text{ m/s}^2$  (graph b) and scaled at  $5\text{m/s}^2$  (graph  
1267 d).

1268 **Figure 10 :** Comparison of the acceleration pseudo-response spectra at the ground surface, for the non-  
1269 linear computations using the high frequency input motion scaled to  $0.5 \text{ m/s}^2$  (graph a) and scaled  
1270 at  $5\text{m/s}^2$  (graph c) and using the low-frequency input motion scaled to  $0.5 \text{ m/s}^2$  (graph b) and scaled  
1271 at  $5\text{m/s}^2$  (graph d).

1272 **Figure 11 :** Standard deviation (in log unit) of the transfer function (left) and response spectra (right)  
1273 depending of the input motion used.

1274 **Figure 12** : Peak shear strain profiles reached at each depth by each team for the high and low frequency  
1275 reference motion scaled at the highest PGA level ( $5 \text{ m/s}^2$ ), for the profile 1 and for rigid substratum  
1276 conditions.

1277 **Figure 13** : Standard deviation (in  $\log_{10}$  unit) of the PGA at the surface of the P1 profile, for the 5 different  
1278 computational cases (linear –elastic, linear visco-elastic, non-linear with input motion scaled to the  
1279 lowest ( $0.5 \text{ m/s}^2$ ), medium ( $1 \text{ m/s}^2$ ) and highest ( $5 \text{ m/s}^2$ ) PGA, for the pulse-like, the high frequency  
1280 and the low frequency content motions. The left sub-plot shows the results for the rigid substratum  
1281 case and the right sub-plot for the elastic substratum.

1282 **Figure 14** : Standard deviation (in log unit) of the different intensity parameters for the P1 profile, for the  
1283 5 different computational cases (linear –elastic, linear visco-elastic, non-linear with input motion  
1284 scaled to the lowest ( $0.5 \text{ m/s}^2$ ), medium ( $1 \text{ m/s}^2$ ) and highest ( $5 \text{ m/s}^2$ ) PGA, for the low frequency  
1285 content motion. The left sub-graph shows the results for the rigid substratum case and the right sub-  
1286 graph for the elastic substratum.

1287 **Figure 15** : Standard deviation (in log unit) of the PGA for the profile 1 2 and 3, for the 5 different  
1288 computational cases (linear –elastic, linear visco-elastic, non-linear with input motion scaled to the  
1289 lowest

1290 **Figure 16** : Stress-strain curves at the bottom of P1 Profile for the Rigid substratum case subjected to the  
1291 low frequency motion (in color and the high frequency motion in black scaled to the highest PGA  
1292 ( $5 \text{ m/s}^2$ ). The thicker curves are for code/team couples that exceed the specified shear strength of  
1293  $65 \text{ KPa}$ , whereas the thin curves represent the code/team couples that use  $65 \text{ KPa}$ . The lighter  
1294 curves are for codes using damping control and the darker curves the others.

1295 **Figure 17** : Standard deviation values ( $\sigma_{\log}$ , in  $\log_{10}$  units) of four parameters for the non-linear  
1296 computation using the low-frequency content input motion scaled to the highest PGA : PGA (a),  
1297 Response spectra at  $0.27 \text{ s}$  (b), Response spectra at  $0.09 \text{ s}$  (c) all three at the surface of P1 and the  
1298 maximal shear deformation at the bottom of the P1 profile (d). The standard deviation are given for  
1299 each group of the four groupings: depending on their low strain attenuation implementation (G-1)  
1300 their numerical scheme (G-2) their constitutive models (G-3) and their values of shear strength at  
1301 the bottom of P1 and use of damping control or not (G-5). The dotted grey line illustrates the  
1302 standard deviation for all code/team couples.

1303 **Figure 18** : Comparison of the pseudo- acceleration response spectra at the ground surface of P1 with  
1304 rigid substratum condition, for the non-linear computation using for (a) and (c) graphs the high  
1305 frequency input motion and for (b) and (d) graphs the low-frequency input motion and with for the  
1306 (a) and (b) graphs the middle input motion PGA and the (c) and (d) graphs the highest input motion  
1307 PGA. The response spectra were sorted according to three groups: group 1 is composed of the  
1308 code/team couples using similar  $\tau_{max}$  and damping control constitutive model. Group 2 use similar  
1309  $\tau_{max}$  and no damping control and Group 3 are the other code team couples. The standard deviation  
1310 for each sub-group is compared to the standard deviation using all results in the upper graphs, the  
1311 figures indicate the number of simulations that are in each group.

1312

1313